The Astronomical Journal, 127:1285–1304, 2004 March

FAINT 6.7 MICRON GALAXIES AND THEIR CONTRIBUTIONS TO THE STELLAR MASS DENSITY IN THE UNIVERSE[1]

Yasunori Sato,[2,3] Lennox L. Cowie,[4] Kimiaki Kawara,[3] Hideo Matsuhara,[5] Haruyuki Okuda,[6] David B. Sanders,[4,7] Yoshiaki Sofue,[3] Yoshiaki Taniguchi,[8] and Ken-ichi Wakamatsu[9]

Received 2002 August 5; accepted 2003 December 3

ABSTRACT

We discuss the nature of faint 6.7 μm galaxies detected with the mid-infrared camera ISOCAM on board the *Infrared Space Observatory* (*ISO*). The 23 hr integration on the Hawaii Deep Field SSA13 has provided a sample of 65 sources down to 6 μJy at 6.7 μm. For 57 sources, optical or near-infrared counterparts were found using a statistical method. All four *Chandra* sources, three SCUBA sources, and one VLA/FIRST source in this field were detected at 6.7 μm with high significance. Using their optical to mid-infrared colors, we divided the 6.7 μm sample into three categories: low-redshift galaxies with past histories of rapid star formation, high-redshift ancestors of these, and other star-forming galaxies. Rapidly star-forming systems at high redshifts dominate the faintest end. Spectroscopically calibrated photometric redshifts were derived from fits to a limited set of template spectral energy distributions (SEDs). They show a high-redshift tail in their distribution with faint (<30 μJy) galaxies at $z > 1$. The 6.7 μm galaxies tend to have brighter K magnitudes and redder $I-K$ colors than the blue dwarf population at intermediate redshifts. Stellar masses of the 6.7 μm galaxies were estimated from their rest-frame, near-infrared luminosities. Massive galaxies ($M_{\rm star} \sim 10^{11}$ $M_{\odot}$) were found in the redshift range of $z = 0.2$–3. Epoch-dependent stellar mass functions indicate a decline of massive galaxies' comoving space densities with redshift. Even with such a decrease, the contributions of the 6.7 μm galaxies to the stellar mass density in the universe are found to be comparable to those expected from UV bright galaxies detected in deep optical surveys.

Key words: cosmology: observations — galaxies: evolution — galaxies: luminosity function, mass function — galaxies: stellar content — infrared: galaxies — surveys

1. INTRODUCTION

The evolution of galaxies can be traced in their spectral energy distributions (SEDs) as a result of the aging and accumulation of stellar populations. Because more massive stars evolve faster, ultraviolet (UV) emission becomes relatively weaker as time elapses, provided that no further star formation occurs. This sensitivity to ongoing star formation can be used to trace the star formation history in galaxies; however, UV light suffers from dust extinction. Thus, optical observations of the redshifted UV emission from distant galaxies require undesirable corrections if we are to deduce the evolution of their star-forming activity.

However, if we observe galaxies at a longer wavelength, this situation is improved. At rest-frame near-infrared wavelengths, much of the emission originates from low-mass stars. Their lifetime is comparable to the age of the universe; thus, the effect of aging is much milder than that in the UV. The complicating effects of dust extinction are almost negligible at this wavelength. Most of the changes in the near-infrared SEDs are caused by the accumulation of stellar populations in galaxies. These facts ensure good accuracy in estimating the stellar masses of galaxies from their near-infrared luminosities.

Stellar mass is one of the most fundamental properties of galaxies. This motivates the undertaking of galaxy surveys in the near-infrared. For distant galaxies, very sensitive surveys should be performed at a longer wavelength in order to detect their rest-frame near-infrared light. The mid-infrared camera ISOCAM (Cesarsky et al. 1996) on board the *Infrared Space Observatory* (*ISO*; Kessler et al. 1996) can fulfill these requirements for the first time.

Most of the deep ISOCAM surveys have utilized two broadband filters: LW2 (5–8.5 μm) at 6.7 μm and LW3 (12–18 μm) at 15 μm (Serjeant et al. 1997; Taniguchi et al. 1997; Flores et al. 1999a, 1999b; Altieri et al. 1999; Oliver et al. 2002). In particular, those at 15 μm have attracted much interest (Genzel & Cesarsky 2000; Franceschini et al. 2001, 2003), mainly because of the discovery of a strongly evolving population of galaxies below 1 mJy (Elbaz et al. 1999). The excess could be explained by a large number of star-forming galaxies at $z \sim 1$.

The 6.7 μm cosmological observations with ISOCAM attracted less attention since they resulted in generally fewer detections than at 15 μm. This may be because such observations sample a dip in galaxy SEDs between stellar and hot dust emission. The passband of the LW2 filter matches the location of the unidentified infrared-band (UIB) emission in

[1] Based on observations with *ISO*, an ESA project with instruments funded by ESA Member States (especially the PI countries: France, Germany, the Netherlands, and the United Kingdom) and with the participation of ISAS and NASA.

[2] Japan Society for the Promotion of Science (JSPS) Research Fellow.
[3] Institute of Astronomy, University of Tokyo, 2-21-1 Osawa, Mitaka, Tokyo, 181-0015 Japan; ysato@ioa.s.u-tokyo.ac.jp.
[4] Institute for Astronomy, University of Hawaii, 2680 Woodlawn Drive, Honolulu, HI 96822.
[5] Institute of Space and Astronautical Science (ISAS), Japan Aerospace Exploration Agency, 3-1-1 Yoshinodai, Sagamihara, Kanagawa, 229-8510 Japan.
[6] Gunma Astronomical Observatory, 6860-86 Nakayama, Takayama, Agatsuma, Gunma, 377-0702 Japan.
[7] Max-Planck-Institut für extraterrestrische Physik, Postfach 1317, D-85740 Garching, Germany.
[8] Astronomical Institute, Graduate School of Science, Tohoku University, Aramaki, Aoba, Sendai, 980-8578 Japan.
[9] Faculty of Engineering, Gifu University, 1-1 Yanagido, Gifu, 501-1193 Japan.

the local universe. Such dust emission shifts away from the passband with redshift (Aussel et al. 1999). At high redshifts, $z > 1$, the major contribution to the LW2 band becomes stellar emission from galaxies. However, detection of such emission from distant galaxies requires extremely high sensitivities. Based on the importance of detecting near-infrared stellar emission from high-redshift galaxies for estimating their stellar masses, we conducted a very deep 6.7 μm survey in the Hawaii Deep Field SSA13 (Sato et al. 2003). The 1 σ sensitivity reached 3 μJy, which is smaller than the published values of 7 μJy in Taniguchi et al. (1997) and Aussel et al. (1999). Most recently, Metcalfe et al. (2003) reached a depth similar to ours using a massive cluster lens. In this paper, we discuss insights deduced from the faint 6.7 μm galaxies detected in the SSA13 field.

After describing the 6.7 μm sample in § 2, we discuss the identification of multiwavelength counterparts in § 3. In § 4, the nature of the identified galaxies is examined with the GRASIL star/dust SED model (Silva et al. 1998). In § 5, their stellar masses are obtained using the rest-frame near-infrared luminosities. We also discuss the evolution of the stellar mass function and the stellar mass density in the universe. Finally, we present a discussion in § 6 and conclusions in § 7. Throughout this paper, we assume a flat universe with $\Omega_M = 0.3$, $\Omega_\Lambda = 0.7$, and $H_0 = 65$ km s^{-1} Mpc^{-1}. All optical and near-infrared magnitudes in this paper are in the Vega system.

2. THE 6.7 μm SAMPLE

A deep mid-infrared survey has been conducted with the ISOCAM array on board the *ISO*. The broadband filter LW2 (5–8.5 μm) with a reference wavelength of 6.7 μm was used to image a high Galactic latitude region in the Hawaii Deep Field SSA13. Many raster observations totaling an observing time of 23 hr were combined to give a map with a nominal areal coverage of 16 arcmin^2 with a beam FWHM of 7.″2. Details of the observations are given in Sato et al. (2003).

With a nonuniform noise distribution over the map, source detections were performed using a signal-to-noise ratio (S/N) map. The noise map was created from the standard deviations of the co-added raster images at each pixel. Detection parameters were determined by comparing numbers of detected sources at the positive and negative sides of the map ($N_{\rm pos}$ and $N_{\rm neg}$, respectively) with the same detection parameter set. We have chosen the parameter set giving the largest $N_{\rm pos} - N_{\rm neg}$, where $N_{\rm pos} = 65$ and $N_{\rm neg} = 12$. Total 6.7 μm fluxes of the positive sources resulted in a range from 6 to 170 μJy (Table 1).

By setting a threshold that can exclude all the negative sources, we extracted a subsample of the positive sources. This subsample, the primary sample, consists of 33 sources having total fluxes larger than 12 μJy and detection S/Ns larger than 4.3 (Table 1). Because there should be no effects from spurious detections in the primary sample, our main results are deduced based on the primary sample. No corrections for the contamination of fake sources are necessary for the primary sample to derive integrated quantities such as stellar mass functions and stellar mass densities discussed in § 5. In fact, galaxy number counts shown in Sato et al. (2003) were obtained only with the primary sample.

The remaining 32 positive sources are put into the supplementary sample. For the number of negative sources ($N_{\rm neg} = 12$) having comparably low significance values, the number of true sources in the supplementary sample could be 20. However, we expect that more sources in the supplementary sample are real. This is because the adopted image processing could produce negative ghosts around bright sources, and at least three of the negative sources were identified as such (Sato et al. 2003). Genuine sources in the supplementary sample should provide meaningful information on the 6.7 μm sources, especially at the faintest flux levels. Some of them are mentioned in the following sections with a caveat that there are some effects from spurious sources.

In Table 1, sources in both samples are listed. Here we also show the 12 negative sources as the negative sample. All are examined using the source identification procedure given in § 3.

3. SOURCE IDENTIFICATION

Counterparts of the 6.7 μm sources were searched at multiple wavelengths, from the X-ray to the radio. We used two identification methods, the probability ratio method in the optical and near-infrared, and the nearest neighbor search at X-ray, submillimeter, and radio wavelengths. The results are summarized in Tables 1 and 2, respectively.

3.1. *Optical and Near-Infrared Identifications*

3.1.1. *The Identification Procedure*

Optical and near-infrared counterparts of the 6.7 μm sources were sought in the *K*, *I*, and *B* bands. Data from these three bands were taken from the ground (Cowie et al. 1996), but we utilized a *Hubble Space Telescope* (*HST* WFPC2 catalog in the I_{814} band as well (Cowie, Hu, & Songaila 1995). The catalog limits were estimated as $K = 19.9$, $I_{814} = 24.7$, $I = 23.7$, and $B = 25.5$ (3 σ). Photometric uncertainties were derived by summing relative and absolute uncertainties quadratically. Absolute photometric uncertainties were estimated to be 0.1 mag for corrected aperture magnitudes (Cowie et al. 1994). We do not distinguish between I_{814} and *I* magnitudes in the following, because they do not show significant differences for the sources in our sample. At these magnitude limits, surface densities become higher than that of the 6.7 μm sources. We therefore introduced two probabilities to evaluate whether a candidate counterpart of magnitude m_1 at distance r_1 should be considered as a true association (Mann et al. 1997; Flores et al. 1999a).

Even for a true association between sources at two wavelengths, there is expected to be a certain amount of displacement in their positions. If we can neglect differences in light profiles at the two wavelengths, a major cause of the displacement is measurement error at both wavelengths. Based on smaller beam sizes in the optical and near-infrared ($\sim$1″ or less), we only took into account measurement errors in the 6.7 μm coordinates. With an assumption that the errors follow a Gaussian distribution, the probability for a true association P_t is defined as

$$P_t = 1 - \sqrt{\frac{2}{\pi}} \int_0^\alpha \exp\left(-\frac{x^2}{2}\right) dx, \qquad (1)$$

where $\alpha (= r_1/r_0)$ is the displacement of a potential counterpart normalized to the 1 σ positional accuracy r_0 of the 6.7 μm source in question. This r_0-value was determined with Monte Carlo simulations by Sato et al. (2003).

As long as the displacement has a finite value r_1, we cannot exclude the possibility that an irrelevant source will be found

TABLE 1

SOURCE IDENTIFICATIONS IN THE OPTICAL AND NEAR-INFRARED

Name	R.A. (J2000.0)	Decl. (J2000.0)	r_0 (arcsec)	6.7 μm (μJy)	S/N	ID	r_1 (arcsec)	P_t	P_c	P_t/P_c	$P_t/P_c^{(2)}$
					Primary Sample						
3.....	13 12 18.09	+42 43 45.0	1.1	50	11.4	*K*	0.8	0.49	0.000056	880.	...
6.....	13 12 18.32	+42 43 19.2	1.1	66	11.9	*K*	0.5	0.63	0.000038	1700.	...
9.....	13 12 19.48	+42 45 36.4	1.5	25	5.8	*K*	0.5	0.75	0.00069	110.	...
10.....	13 12 20.01	+42 44 38.4	1.4	21	6.4	*K*	0.7	0.64	0.0015	41.	...
11.....	13 12 21.02	+42 44 33.8	1.5	19	5.9	*K*	1.0	0.49	0.00094	53.	3.7
13.....	13 12 21.39	+42 44 23.4	1.4	24	7.0	*K*	0.3	0.80	0.000092	870.	...
14.....	13 12 21.57	+42 44 05.8	1.5	19	6.3	*K*	0.8	0.58	0.0023	25.	...
15.....	13 12 21.58	+42 45 18.8	1.0	60	15.6	*K*	0.3	0.77	0.000086	900.	...
16.....	13 12 21.89	+42 43 45.5	1.5	19	5.8	*K*	2.3	0.12	0.031	3.8	...
17.....	13 12 22.53	+42 44 50.9	1.5	17	5.3	*K*	0.3	0.86	0.00053	160.	0.14
20.....	13 12 23.65	+42 45 16.9	1.5	20	6.2	*K*	2.9	0.048	0.032	1.5	...
22.....	13 12 23.91	+42 45 43.5	0.9	135	28.5	*K*	1.1	0.25	0.0000023	11000.	...
25.....	13 12 24.90	+42 44 14.8	1.1	39	11.7	*K*	2.5	0.023	0.0014	16.	...
27.....	13 12 25.2	+42 46 00	1.2	45	10.1	...	...	...	...	...	...
28.....	13 12 25.18	+42 43 44.9	1.3	27	7.9	*K*	1.3	0.34	0.0042	82.	2.8
30.....	13 12 26.31	+42 42 26.9	1.6	70	5.0	*I*	0.9	0.59	0.000025	2300.	...
33.....	13 12 27.32	+42 44 49.7	1.5	17	5.4	*K*	1.4	0.36	0.0087	41.	0.032
35.....	13 12 27.70	+42 45 36.6	1.7	15	4.8	*K*	1.3	0.44	0.0059	75.	...
39.....	13 12 28.44	+42 46 03.3	1.5	27	5.4	*I*	1.4	0.35	0.0078	45.	...
40.....	13 12 28.29	+42 44 54.6	1.7	14	4.8	*K*	3.4	0.047	0.084	0.56	...
41.....	13 12 28.58	+42 43 58.9	1.1	46	13.3	*K*	1.0	0.37	0.00016	240.	...
44.....	13 12 29.21	+42 45 58.2	1.3	37	8.2	*I*	1.1	0.42	0.00032	130.	...
47.....	13 12 29.88	+42 44 08.5	1.5	16	5.3	*K*	0.7	0.64	0.00049	130.	0.19
49.....	13 12 30.10	+42 44 20.7	1.6	15	5.0	*K*	1.3	0.42	0.0071	60.	0.14
50.....	13 12 30.16	+42 44 56.5	1.5	19	5.8	*K*	2.4	0.11	0.015	7.3	0.11
51.....	13 12 31.05	+42 43 32.6	1.4	22	6.7	*K*	0.6	0.66	0.00025	260.	...
54.....	13 12 31.50	+42 45 52.2	0.9	167	23.6	*K*	1.2	0.20	0.000095	210.	...
55.....	13 12 31.90	+42 43 46.4	1.9	12	4.3	*K*	2.1	0.25	0.010	25.	...
57.....	13 12 31.94	+42 44 29.7	1.5	18	6.2	*K*	2.2	0.13	0.033	3.9	...
59.....	13 12 33.92	+42 44 42.7	1.6	18	5.0	*K*	1.2	0.47	0.00099	47.	20.
61.....	13 12 34.68	+42 43 42.8	1.3	55	8.3	*K*	2.5	0.058	0.0024	24.	...
62.....	13 12 34.51	+42 43 09.3	1.8	88	4.5	*I*	2.1	0.25	0.00056	45.	...
64.....	13 12 35.90	+42 43 58.0	1.3	107	7.7	*B*	2.0	0.14	0.000074	190.	...
					Supplementary Sample						
0.....	13 12 15.79	+42 44 00.3	2.5	19	2.7	*K*	0.6	0.80	0.00013	600.	...
1.....	13 12 16.8	+42 44 21	1.9	18	4.1	...	...	...	...	...	...
2.....	13 12 17.10	+42 44 52.2	2.3	14	3.0	I_{814}	3.1	0.18	0.11	1.6	0.17
4.....	13 12 17.82	+42 45 27.3	2.3	18	3.2	*K*	2.6	0.25	0.044	5.6	...
5.....	13 12 18.1	+42 46 15	2.6	34	2.7	...	...	...	...	...	...
7.....	13 12 18.7	+42 42 48	2.3	66	3.0	...	...	...	...	...	...
8.....	13 12 19.34	+42 45 01.1	1.9	12	4.0	*K*	2.0	0.29	0.0065	44.	...
12.....	13 12 21.19	+42 46 26.0	2.3	63	3.0	*I*	2.0	0.39	0.015	26.	4.0
18.....	13 12 22.45	+42 43 15.6	2.7	8	2.6	*K*	4.1	0.14	0.062	2.2	...
19.....	13 12 23.10	+42 46 05.4	2.2	17	3.3	*K*	1.9	0.39	0.0067	58.	...
21.....	13 12 23.30	+42 44 29.4	2.3	9	3.0	I_{814}	2.3	0.31	0.081	3.9	2.1
23.....	13 12 24.18	+42 43 57.7	2.3	9	3.1	*K*	2.0	0.39	0.022	18.	...
24.....	13 12 24.33	+42 43 23.9	2.0	12	3.8	I_{814}	2.0	0.31	0.078	3.9	0.067
26.....	13 12 24.60	+42 45 11.4	2.1	10	3.5	*K*	2.2	0.29	0.023	13.	...
29.....	13 12 25.56	+42 43 20.5	2.4	8	2.8	*I*	2.4	0.33	0.016	20.	8.5
31.....	13 12 26.58	+42 45 30.0	3.2	6	2.4	I_{814}	5.2	0.11	0.086	1.2	0.43
32.....	13 12 26.31	+42 44 04.8	2.1	9	3.4	*K*	1.3	0.55	0.011	48.	1.5
34.....	13 12 27.51	+42 46 30.4	2.4	45	2.9	*I*	2.0	0.40	0.017	23.	4.1
36.....	13 12 27.80	+42 45 09.6	2.4	8	2.8	*K*	1.0	0.66	0.0053	13.	0.24
37.....	13 12 27.9	+42 42 20	2.4	87	2.9	...	...	...	...	...	...
38.....	13 12 28.50	+42 44 28.9	2.1	10	3.6	*K*	2.6	0.23	0.0078	29.	7.0
42.....	13 12 28.9	+42 46 19	2.3	32	3.1	...	...	...	...	...	...
43.....	13 12 28.87	+42 43 04.8	2.1	12	3.7	*I*	2.5	0.23	0.021	11.	0.070
45.....	13 12 29.20	+42 44 38.7	3.0	7	2.5	*K*	2.5	0.39	0.020	20.	3.5
46.....	13 12 29.69	+42 43 00.1	2.3	11	3.2	*I*	1.1	0.63	0.0072	88.	2.0
48.....	13 12 29.9	+42 45 14	2.3	9	3.1	...	...	...	...	...	...
52.....	13 12 31.76	+42 42 42.7	2.3	24	3.2	*I*	3.4	0.14	0.066	2.2	0.34

TABLE 1—*Continued*

Name	R.A. (J2000.0)	Decl. (J2000.0)	r_0 (arcsec)	6.7 μm (μJy)	S/N	ID	r_1 (arcsec)	P_t	P_c	P_t/P_c	$P_t/P_c^{(2)}$
53.....	13 12 31.5	+42 42 36	2.9	27	2.5	...	...	...	...	...	...
56.....	13 12 31.86	+42 45 04.1	2.4	8	2.9	*K*	1.4	0.55	0.0080	68.	...
58.....	13 12 32.78	+42 43 12.4	2.6	15	2.7	*I*	1.6	0.53	0.018	29.	16.
60.....	13 12 34.31	+42 46 00.3	3.3	26	2.3	*I*	2.4	0.47	0.012	38.	5.9
63.....	13 12 34.81	+42 45 05.1	2.1	18	3.7	*K*	2.6	0.21	0.017	12.	...
				Negative Sample							
N0.....	13 12 17.9	+42 45 11	2.2	−17	−3.3	...	...	...	...	...	...
N1.....	13 12 19.5	+42 45 47	2.2	−13	−3.4	...	...	...	...	...	...
N2.....	13 12 20.0	+42 43 33	3.3	−6	−2.3	...	...	...	...	...	...
N3.....	13 12 23.6	+42 45 28	2.1	−10	−3.4	...	...	...	...	...	...
N4.....	13 12 24.8	+42 44 37	2.6	−7	−2.6	...	...	...	...	...	...
N5.....	13 12 25.5	+42 42 04	2.2	−125	−3.3	...	...	...	...	...	...
N6.....	13 12 30.5	+42 45 37	1.9	−11	−4.0	...	...	...	...	...	...
N7.....	13 12 31.46	+42 44 26.0	2.0	−11	−3.8	I_{814}	2.9	0.15	0.085	1.7	1.3
N8.....	13 12 32.9	+42 45 13	2.3	−9	−3.2	...	...	...	...	...	...
N9.....	13 12 34.23	+42 43 27.3	3.3	−17	−2.3	*I*	2.3	0.49	0.037	13.	1.7
N10.....	13 12 35.76	+42 44 43.7	2.0	−26	−3.9	*I*	4.2	0.032	0.0067	4.7	0.15
N11.....	13 12 38.7	+42 44 38	3.3	−69	−2.3	...	...	...	...	...	...

NOTES.—Source identification results from the probability ratio method described in § 3.1. The contents are divided into three subsamples; the primary, supplementary, and negative samples (§ 2). Names, coordinates, their 1 σ errors (r_0) and total 6.7 μm fluxes are extracted from Sato et al. 2003. The coordinates of the successfully identified sources are updated with their optical or near-infrared positions in the identifying image, which is indicated in the ID column. Listed S/Ns are derived from standard deviations of the co-added images at the source position using a 7.″2 aperture. Thus, both photon noise and undersampling effects are included. With raster observations, pixel values could range from $\sim$25% to $\sim$100% of source fluxes depending on the exact locations of the sources on the ISOCAM 6″ pixels, giving high standard deviations at source positions. At 6.7 μm, an Airy disk size is 5.″6 for the *ISO* telescope. Note that errors in total 6.7 μm fluxes are much larger than can be inferred from these detection S/N values. Derivation of total fluxes and their associated errors are described in Sato et al. 2003. For each identification, we list the distance between the 6.7 μm source and the identified source in the ID image (r_1). Two probabilities that the identified source is a true association (P_t) or a chance association (P_c), and their ratios are also shown. The last column shows the second highest probability ratio for sources within a distance of $3r_0$ from the original 6.7 μm position. The contents for the negative sample are the same but with negative flux and S/N values. Units of right ascension are hours, minutes, and seconds, and units of declination are degrees, arcminutes, and arcseconds.

at a distance smaller than r_1. Such a chance event should follow Poisson statistics for an area of πr_1^2. Then the probability for a chance association P_c is derived as

$$P_c = 1 - \exp\left[-\pi r_1^2 N(<m_1)\right], \quad (2)$$

where $N(<m_1)$ is the surface density of optical or near-infrared sources with magnitudes brighter than m_1, the magnitude of a potential counterpart. Because only two stars are expected in this 6.7 μm sample (Sato et al. 2003), $N(<m_1)$ was derived by integrating differential galaxy counts shown in Metcalfe et al. (2001) and Maihara et al. (2001).

These two probabilities, P_t and P_c, were calculated for all potential counterparts up to a distance of $3r_0$ from each 6.7 μm position. The large search radius was necessary to take account of the large uncertainty in the determination of r_0 (Sato et al. 2003). We then selected an optical or near-infrared counterpart having the highest ratio of P_t/P_c. If there is no candidate source with $P_t/P_c > 1$, the 6.7 μm source was regarded as unidentified. Assuming that SEDs of the 6.7 μm sources are smoothly connected, we performed the identification procedure starting from the nearest wavelength. The adopted *K*- and I_{814}-band catalogs do not cover the full 6.7 μm field. To take into account the deeper limit of the I_{814}-band catalog, the identification scheme was then set from the *K*, I_{814}, and *I* bands to the *B* band. If the identification at a particular band resulted in a success, counterparts at the shorter wavelengths were sought with a nearest neighbor search. A search of up to 1.″4 turned out to be enough.

3.1.2. *Identification Results*

Of 65 positive sources, 57 were identified in the optical or near-infrared. Figure 1 shows their appearances at the wavelength where the probability calculations were performed. In Table 1, identification band (ID), distance (r_1), two probabilities (P_t and P_c), and their ratio are listed. The coordinates of the identified sources have been updated with those of the optical or near-infrared counterparts. We also show the second-highest ratio of P_t/P_c ($P_t/P_c^{(2)}$) if other candidates were found in the search radius. There are relatively few cases of ambiguous identifications (i.e., where the second largest P_t/P_c is on the same order of magnitude as the largest). In particular, in the primary sample only one source (No. 59) seems to fall into this category. In the following, the identification results for the primary and supplementary samples are examined separately.

For the primary sample, we found that many sources were identified in the *K* band. All the sources that were identified at shorter wavelengths have large P_t/P_c values. As indicated in Table 3, they either lack *K* data (30, 39, and 62) or have blue colors (44 and 64). Sato et al. (2002) identified source 40 with a submillimeter source having a hard X-ray counterpart. This identified source has a smaller significance value ($P_t/P_c \sim 0.6$) than the nominal threshold ($P_t/P_c = 1$) at the *K* band. We regard it as likely that the asymmetric profile of this 6.7 μm source (Sato et al. 2002) affected the probability calculation. The only unidentified source, 27, having a high S/N (=10) lacks *K* data (Table 3) and has a very red mid-infrared–to–optical color.

The lower significance of the supplementary sample leads to poorer positional accuracy ($r_0 \sim 2''$–$3''$), which made the

TABLE 2
SOURCE IDENTIFICATIONS AT THE X-RAY, SUBMILLIMETER, AND RADIO WAVELENGTHS

ISOCAM		*CHANDRA*				SCUBA				VLA		
Name	6.7 μm (μJy)	d_X (arcsec)	Name	2–10 keV (10^{-15}cgs)	0.5–2 keV (10^{-16}cgs)	d_S (arcsec)	Name [BCS99] J13	450 μm (mJy)	850 μm (mJy)	d_R (arcsec)	NAME FIRST J13	1.4 GHz (mJy)
14.....	19	0.8	21	<2.7	7.9	...	...	...	...	...	...	...
17.....	17	1.1	18	4.2	15.	...	...	...	...	...	...	...
20.....	20	...	...	...	...	...	...	...	...	0.2	J131223.6+424517	3.0
28.....	27	...	...	...	...	7.7	J131225.7+424350	<25	2.4	...	...	...
40.....	14	0.5	15	5.7	<4.2	4.7	J131228.0+424458	<25	2.3	...	...	...
57.....	18	...	...	...	...	1.8	J131232.1+424430	<25	3.8	...	...	...
62.....	88	0.3	10	7.8	<3.9	...	...	...	...	...	...	...

NOTES.—Source identifications of the mid-infrared (ISOCAM/LW2) sources in the SSA13 field with X-ray (*Chandra*), submillimeter (JCMT/SCUBA), and radio (VLA/FIRST) sources (Mushotzky et al. 2000; Barger et al. 2001, 1998, 1999; White et al. 1997). Flux limits are nondetections at a level of 3 σ. Listed offsets d_X, d_S, and d_R are measured from the optical or near-infrared positions of the 6.7 μm sources in Table 1.

identifications more difficult. Even in such circumstances, 78% (25/32) of the supplementary sample were identified. Because the supplementary and negative samples have the same S/N level, the identification significance for the supplementary sample can be checked by a comparison with the negative sample. No source in the negative sample was identified in the K band. Thus, the identifications of the supplementary sample in the K band are expected to be robust. Three sources in the negative sample were identified in the I or I_{814} band. However, most of the I- or I_{814}-band identifications in the supplementary sample have better statistics, i.e., larger P_t/P_c values than those for the I- or I_{814}-band identifications in the negative sample. Here I and I_{814} counterparts should be treated separately because of the difference in the catalog depth. The deeper I_{814} sources generally have smaller P_t/P_c values because of the larger surface density of the sources. The I_{814} counterparts for sources 21 and 24 have larger P_t/P_c values than that of the I_{814} counterpart for the negative source N7. The I counterparts for sources 12, 29, 34, 46, 58, and 60 have larger P_t/P_c values than that of the I counterpart for the negative source N9, which has a P_t/P_c value larger than N10. The remaining I- or I_{814}-band identifications are for sources 2, 31, 43, and 52, although most of them have slightly smaller P_t/P_c values than that of their corresponding negative source, N7 or N9. Thus, we expect the number of erroneous identifications in the supplementary sample to be quite small, four at most. The number of unidentified sources in the supplementary sample (7) is comparable to that in the negative sample (9). This indicates that some of the unidentified sources in the supplementary sample could be spurious, especially those detected in noisy regions of the map (e.g., sources 7 and 37). However, some could be very red sources like source 27 in the primary sample.

Flores et al. (1999a) give r_1 and P_c values for the identification of their 6.7 μm sources. Their values are generally larger than ours; the median r_1 is 4.″2 and P_c exceeds 0.3 in some cases. We think that this may be partly due to their neglect of distortion corrections in data processing, which could be as large as one 6″ pixel in size. They adopted 1.″5 map pixels and used only 3–5 sources to determine shifts between images. The median FWHM of 6.7 μm sources on their final map was 11″, while ours was 7.″2. We took into account distortion corrections and used 0.″6 map pixels and 19 reference sources for the image registration (Sato et al. 2003). The differences mentioned above might not explain all of the differences in their identification results, rather, even the sources identified with the least significance in Flores et al. (1999a) have 6.7 μm fluxes larger than ours and corresponding optical magnitudes brighter than ours.

3.2. *X-Ray, Submillimeter, and Radio Identifications*

At the flux levels of the adopted X-ray, submillimeter, and radio catalogs, the surface densities are lower than that of our mid-infrared sample. Thus, source identification at these wavelengths can be achieved using a simple method, a nearest neighbor search.

With the deep *Chandra* observations of SSA13 (Mushotzky et al. 2000), four X-ray sources were detected within the area of the ISOCAM survey. Three of them were detected in the hard X-ray band (2–10 keV) with fluxes larger than 4×10^{-15} ergs s^{-1} cm^{-2}, while two of them were detected in the soft X-ray band (0.5–2 keV) with fluxes larger than 8×10^{-16} ergs s^{-1} cm^{-2} (Table 2). Within 1.″1 of these four X-ray sources, comparable to the positional accuracy of the *Chandra* satellite, we found 6.7 μm counterparts 14, 17, 40, and 62. Here we have used the 6.7 μm coordinates updated with the optical and near-infrared identifications above.

The Submillimetre Common-User Bolometer Array (SCUBA) on the 15 m James Clerk Maxwell Telescope (JCMT) detected three 850 μm sources down to 2 mJy in the deep SCUBA survey of SSA13 (Barger, Cowie, & Sanders 1999). Taking into account the very broad beam at 850 μm (15″ FWHM), all three submillimeter sources were identified with 6.7 μm sources 28, 40, and 57 at distances of up to 7.″7 (Sato et al. 2002). Note that one of the submillimeter sources (40) was also detected in the hard X-ray.

The VLA/FIRST survey at 1.4 GHz detected one 3 mJy source in the 6.7 μm SSA13 map (White et al. 1997). This source is also listed in the VLA/NVSS catalog (Condon et al. 1998). The 6.7 μm counterpart is assigned to source 20 at a distance of 0.″2.

All these X-ray, submillimeter, and radio sources are in the primary sample. Except for one optically bright hard X-ray source, No. 62, they have 6.7 μm fluxes in a range of 10–30 μJy.

4. THE NATURE OF FAINT 6.7 μm GALAXIES

We have identified two stars in the 6.7 μm sample using their image profiles in the optical (Sato et al. 2003). Excluding these stars from the primary sample, we now discuss the nature of the remaining sources, all of which are assumed to be

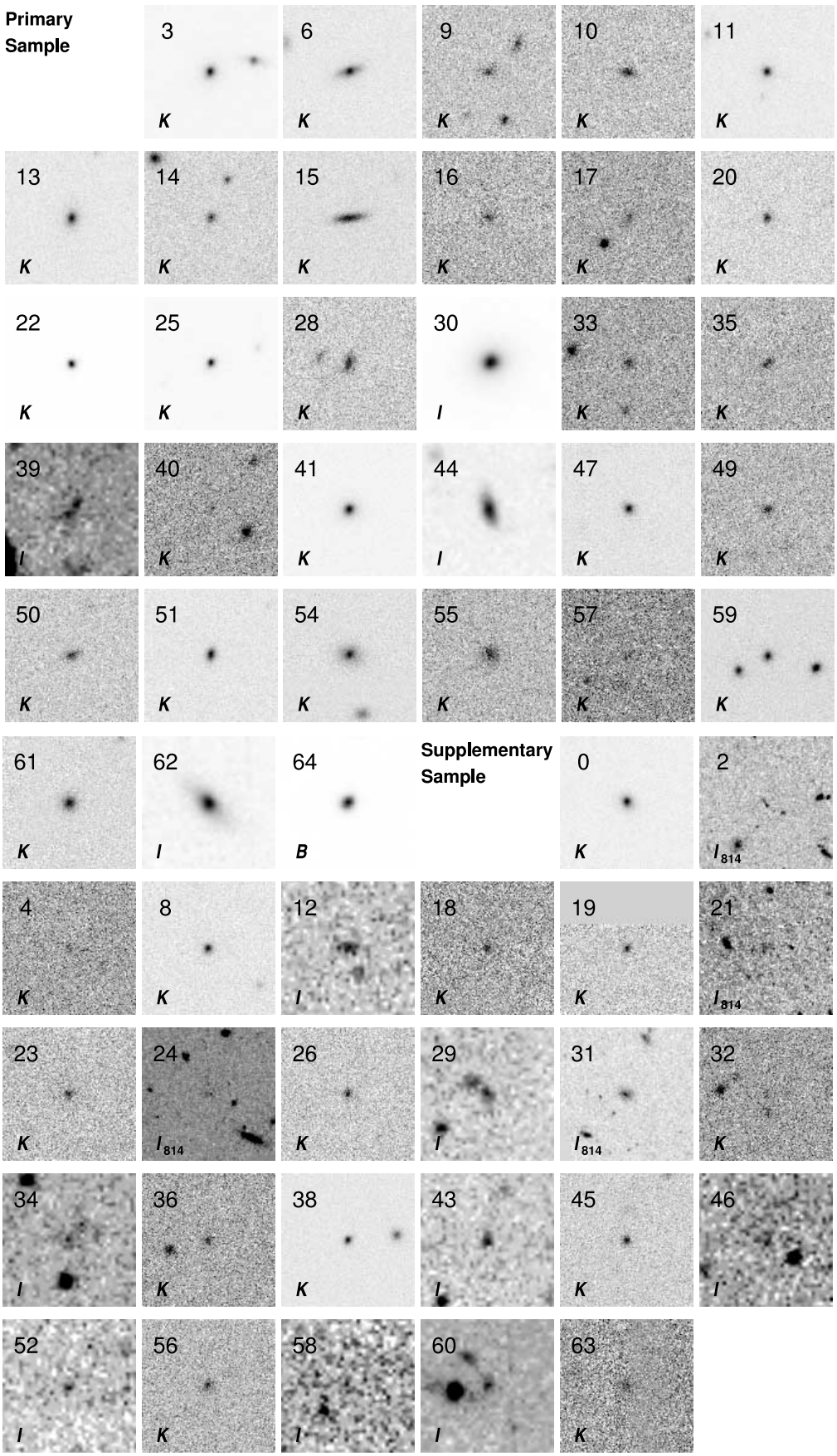

FIG. 1.—Thumbnail images of the identified 6.7 μm sources. The images were taken from the data on which the actual identifications were performed (IDs in Table 1). This imaging band and the name of the 6.7 μm source were overlaid on each $18'' \times 18''$ panel, an area of 3×3 pixels for the ISOCAM $6''$ pixel field-of-view mode. The identified sources were centered in the images. North is up, and east to the left.

TABLE 3

PROPERTIES OF THE MID-INFRARED SOURCES

Name	6.7 μm (μJy)	K (mag)	I (mag)	B (mag)	Type	z_{sp}, z_{ph}	SED_1	χ^2_1	log (M_{star}) (h_{65}^{-2} $M_\odot$)	SED_2	χ^2_2
Primary Sample											
3.....	50	15.8	18.7	22.1	I	0.314	...	...	$11.16^{+0.04}_{-0.06}$	E 8	4.7 (d4/4)
6.....	66	16.1	19.0	22.1	I	0.313	...	...	$11.08^{+0.04}_{-0.09}$	Sa 10	2.2 (d4/4)
9.....	25	18.7	22.6	24.7	II	$1.31^{+0.17}_{-0.15}$	Sb 8	0.0 (d4/4)	$11.39^{+0.13}_{-0.17}$	Sa 5	0.6 (d4/4)
10.....	21	18.8	22.7	>25.5	II	0.914	...	...	$10.89^{+0.06}_{-0.09}$	Sa 6	8.5 (d3/4)
11.....	19	17.4	20.3	24.6	I	0.732	...	...	$11.09^{+0.15}_{-0.05}$	E 3	2.4 (d4/4)
13.....	24	17.3	20.6	24.5	I	0.479	...	...	$10.99^{+0.04}_{-0.08}$	E 8	13.7 (d4/4)
14.....	19	18.9	22.0	23.6	III	1.305	...	...	$11.05^{+0.13}_{-0.16}$	Sa 2	0.1 (d4/4)
15.....	60	17.4	20.1	22.3	III	0.279	...	...	$10.27^{+0.09}_{-0.07}$	Sb 6	2.0 (d4/4)
16.....	19	19.6	22.3	23.9	III	1.168	...	...	$10.96^{+0.13}_{-0.22}$	Sb 3	2.9 (d4/4)
17.....	17	19.9	24.5	>25.5	II	$2.12^{+1.64}_{-0.46}$	Sb 8	0.0 (d3/4)	$11.22^{+0.18}_{-0.18}$	E 1.5	1.2 (d3/4)
20.....	20	19.0	23.0	>25.5	II	$1.16^{+0.15}_{-0.10}$	Arp 220	0.3 (d3/4)	$11.28^{+0.14}_{-0.17}$	E 4	1.8 (d3/4)
22.....	135	13.8	<17.0	18.6	Star	0.000	...	...	...	...	...
25.....	39	16.4	19.1	22.4	I	$0.24^{+0.03}_{-0.03}$	Sa 15	0.1 (d4/4)	$10.75^{+0.04}_{-0.09}$	Sa 11	4.3 (d4/4)
27.....	45	...	>23.7	>25.5	II	...	...	...	...	...	...
28.....	27	18.5	21.6	24.3	III	1.038	...	...	$11.26^{+0.12}_{-0.21}$	Sb 6	11.4 (d5/6)
30.....	70	...	18.2	21.4	I	0.277	...	...	$11.11^{+0.11}_{-0.15}$	E 8	0.1 (d3/3)
33.....	17	19.2	23.7	>25.5	II	$1.43^{+0.23}_{-0.22}$	Sb 13	0.0 (d3/4)	$11.28^{+0.14}_{-0.20}$	E 4	0.4 (d3/4)
35.....	15	18.8	22.1	24.6	III	$1.08^{+0.08}_{-0.11}$	Sa 4	0.0 (d4/4)	$10.98^{+0.16}_{-0.19}$	Sa 4	0.0 (d4/4)
39.....	27	...	22.9	25.4	II	$2.96^{+0.38}_{-0.28}$	Sa 2	0.0 (d3/3)	$11.67^{+0.13}_{-0.30}$	Sa 2	0.0 (d3/3)
40.....	14	19.9	24.0	>25.5	II	$2.70^{+0.85}_{-0.49}$	Sb 4	0.2 (d4/6)	$11.32^{+0.14}_{-0.21}$	Sa 2	4.4 (d4/6)
41.....	46	16.2	18.9	22.6	I	0.489	...	...	$11.33^{+0.13}_{-0.09}$	E 5	2.3 (d4/4)
44.....	37	<17.8	20.0	22.2	III	$0.38^{+0.25}_{-0.03}$	Sc 6	0.0 (d3/4)	$10.29^{+0.12}_{-0.10}$	Sc 6	0.0 (d3/4)
47.....	16	17.5	20.5	24.1	I	0.572	...	...	$10.91^{+0.15}_{-0.05}$	E 4	2.9 (d4/4)
49.....	15	19.1	22.8	>25.5	II	$1.05^{+0.11}_{-0.17}$	Arp 220	0.0 (d3/4)	$11.08^{+0.16}_{-0.19}$	Sa 6	1.0 (u1/4)
50.....	19	18.5	21.4	24.3	III	0.612	...	...	$10.70^{+0.05}_{-0.13}$	Sb 8	0.5 (d4/4)
51.....	22	17.2	20.4	23.9	I	0.378	...	...	$10.80^{+0.04}_{-0.09}$	Sa 10	9.5 (d4/4)
54.....	167	15.6	18.4	20.9	III	$0.56^{+0.16}_{-0.26}$	NGC 6946	0.2 (d4/4)	$11.58^{+0.06}_{-0.07}$	Sa 4	2.7 (d4/4)
55.....	12	18.3	20.9	22.9	III	0.839	...	...	$10.71^{+0.08}_{-0.10}$	Sc 4	4.2 (d4/4)
57.....	18	19.7	>24.7	>25.5	II	$1.94^{+0.41}_{-0.09}$	Arp 220	0.0 (d3/6)	$11.03^{+0.37}_{-0.16}$	E 0.1	6.2 (d3/6)
59.....	18	17.2	20.1	23.6	I	0.415	...	...	$10.88^{+0.04}_{-0.08}$	E 8	0.7 (d4/4)
61.....	55	16.8	19.4	21.5	III	0.276	...	...	$10.44^{+0.06}_{-0.07}$	Sa 4	6.6 (d4/4)
62.....	88	...	19.3	22.4	I	0.241	...	...	$10.64^{+0.04}_{-0.10}$	Sa 11	2.1 (d3/3)
64.....	107	<13.7	<17.2	19.4	Star	0.000	...	...	...	...	...
Supplementary Sample											
0.....	19	16.7	19.5	22.7	I	0.314	...	...	$10.84^{+0.04}_{-0.09}$	Sa 10	3.6 (d4/4)
1.....	18	>19.9	>24.7	>25.5	II	...	...	...	...	...	...
2.....	14	>19.9	24.4	>25.5	II	$2.23^{+2.78}_{-0.81}$	Sa 4	0.0 (d2/4)	$11.27^{+0.18}_{-0.27}$	Sa 3	0.3 (d2/4)
4.....	18	19.7	24.1	>25.5	II	$2.18^{+1.92}_{-0.52}$	Sb 6	0.0 (d3/4)	$11.39^{+0.18}_{-0.27}$	Sa 3	1.1 (u1/4)
5.....	34	...	>23.7	>25.5	II	...	...	...	...	...	...
7.....	66	...	>23.7	>25.5	II	...	...	...	...	...	...
8.....	12	17.9	21.7	>25.5	I	1.028	...	...	$10.93^{+0.21}_{-0.20}$	E 3	3.7 (d3/4)
12.....	63	...	22.9	24.5	II	$1.93^{+0.35}_{-0.33}$	Sa 7	0.0 (d3/3)	$11.87^{+0.18}_{-0.30}$	Sa 3	2.0 (d3/3)
18.....	8	19.0	23.6	>25.5	II	$1.06^{+0.15}_{-0.09}$	GE	0.4 (d3/4)	$10.89^{+0.19}_{-0.34}$	E 5	3.2 (d3/4)
19.....	17	18.1	21.7	>25.5	I	$0.76^{+0.08}_{-0.08}$	Sa 15	0.0 (d3/4)	$11.00^{+0.06}_{-0.06}$	E 5	4.2 (d3/4)
21.....	9	>19.9	24.7	>25.5	II	$1.73^{+0.47}_{-0.52}$	Sa 7	0.0 (d2/4)	$11.01^{+0.17}_{-0.28}$	E 3	0.0 (u2/4)
23.....	9	19.5	23.4	>25.5	II	$1.08^{+0.18}_{-0.16}$	Sb 11	0.0 (d3/4)	$10.93^{+0.17}_{-0.30}$	E 5	0.3 (d3/4)
24.....	12	>19.9	25.0	>25.5	II	$2.70^{+3.21}_{-1.03}$	Sb 6	0.0 (d2/4)	$11.18^{+0.17}_{-0.22}$	E 1.5	0.1 (u2/4)
26.....	10	19.2	23.0	>25.5	II	$1.02^{+0.14}_{-0.18}$	Sb 11	0.0 (d3/4)	$10.97^{+0.18}_{-0.25}$	E 5	0.3 (d3/4)
29.....	8	>19.9	22.6	24.2	III	0.620	...	...	$9.26^{+0.20}_{-0.18}$	Sb 1	0.7 (d3/4)
31.....	6	>19.9	22.7	25.6	III	$0.76^{+0.17}_{-0.49}$	Sc 12	0.1 (u1/4)	$10.28^{+0.09}_{-0.25}$	Sb 6	0.3 (u1/4)
32.....	9	19.8	>23.7	>25.5	II	$1.50^{+0.86}_{-0.67}$	GE	0.0 (d2/4)	$10.97^{+0.20}_{-0.24}$	Sa 4	0.0 (u2/4)
34.....	45	...	23.1	24.5	II	$2.09^{+0.35}_{-0.49}$	Sb 6	0.0 (d3/3)	$11.76^{+0.18}_{-0.27}$	Sa 3	0.6 (d3/3)
36.....	8	19.4	24.8	>25.5	II	$1.39^{+0.21}_{-0.24}$	GE	0.9 (d3/4)	$10.96^{+0.19}_{-0.31}$	E 4	4.7 (d3/4)
37.....	87	...	>23.7	>25.5	II	...	...	...	...	...	...
38.....	10	17.6	21.6	>25.5	I	$0.75^{+0.09}_{-0.08}$	Sa 15	9.9 (d3/4)	$11.17^{+0.05}_{-0.09}$	E 5	16.6 (d3/4)
42.....	32	...	>23.7	>25.5	II	...	...	...	...	...	...
43.....	12	...	22.7	25.5	II	$1.07^{+0.14}_{-0.23}$	Sa 7	0.0 (d3/3)	$10.95^{+0.17}_{-0.23}$	Sa 5	0.5 (d3/3)
45.....	7	18.7	22.5	>25.5	I	$0.81^{+0.07}_{-0.10}$	GE	0.9 (d3/4)	$10.85^{+0.06}_{-0.11}$	Sa 7	4.7 (d3/4)
46.....	11	...	23.4	>25.5	II	$3.33^{+1.41}_{-1.19}$	E 0.8	0.0 (d2/3)	$11.25^{+0.21}_{-0.28}$	E 0.8	0.0 (d2/3)
48.....	9	>19.9	>24.7	>25.5	II	...	...	...	...	...	...
52.....	24	...	23.5	>25.5	II	$1.31^{+0.23}_{-0.34}$	GE	0.0 (d2/3)	$11.48^{+0.18}_{-0.28}$	E 5	0.9 (d2/3)

TABLE 3—*Continued*

Name	6.7 μm (μJy)	K (mag)	I (mag)	B (mag)	Type	z_{sp}, z_{ph}	SED$_1$	χ^2_1	log(M_{star}) (h_{65}^{-2} $M_\odot$)	SED$_2$	χ^2_2
53.....	27	...	>23.7	>25.5	II	...	...	...	...	...	...
56.....	8	19.0	22.5	25.2	III	$0.88^{+0.08}_{-0.17}$	M 51	0.1 (d4/4)	$10.78^{+0.07}_{-0.10}$	Sa 6	1.3 (d4/4)
58.....	15	...	23.7	>25.5	II	$1.43^{+0.29}_{-0.46}$	E 5	0.0 (d2/3)	$11.22^{+0.19}_{-0.30}$	E 4	0.0 (d2/3)
60.....	26	...	22.2	24.0	III	$1.33^{+0.15}_{-1.23}$	Sc 10	0.0 (d3/3)	$11.29^{+0.22}_{-0.32}$	Sa 3	0.1 (d3/3)
63.....	18	18.4	23.4	>25.5	II	$1.22^{+0.21}_{-0.11}$	GE	0.3 (d3/4)	$11.32^{+0.17}_{-0.25}$	E 5	5.4 (d3/4)

NOTES.—Properties of the primary and supplementary 6.7 μm samples. Magnitudes at the K, I, and B bands are corrected total magnitudes as in Cowie et al. 1996. Measurements with a 3″ aperture are corrected with an average offset. Upper flux limits are nondetections at a level of 3 σ. Lower flux limits are real measurements for saturated sources or for sources at the image boundaries. Except for two stars, the sources are divided into three color types (§ 4.1) using the GRASIL SED library (Appendix). Spectroscopic redshifts z_{sp} (Songaila et al. 1994; Cowie et al. 1996; Barger et al. 2001) are listed with no error information, while photometric redshifts z_{ph} are shown with their 90% confidence limits. Photometric redshifts z_{ph} are derived with fits to the GRASIL evolving templates and local ones (§ 4.2.1), while stellar masses M_{star} are derived with fits to the GRASIL evolving templates only (§ 5.2). The results of these two fits are shown separately as (SED$_1$, χ^2_1) and (SED$_2$, χ^2_2). The name of the best-fit SED is listed with its age in gigayears for the case of the evolving SED. The local template for giant elliptical galaxies is marked as GE. Just after the χ^2 value, ancillary information on the fit is shown in parenthesis. For example, d3/4 means that three detections among four photometric data were used to determine the best-fit and the resulting χ^2-value. The remaining one flux limit was checked for its consistency to the fit. In case of u1/4, one upper flux limit (nondetection) was found to be inconsistent with the initial best-fit derived with the remaining three detections. Then the normalization of the initial fit was decreased down to the upper limit, and the χ^2-value was evaluated with this re-normalized spectrum.

galaxies. We utilize the GRASIL star/dust galaxy SED model (Silva et al. 1998), which is explained in some detail in the Appendix.

4.1. *Colors*

With the K-, I-, and B-band photometry, we examined the distributions of faint 6.7 μm galaxies in various color-color plots. In one plot (Fig. 2), we identified a distinct population of faint 6.7 μm galaxies having red $B-I$ colors and low ratios of f_ν(6.7 μm)/f_ν (K). To derive ratios with 6.7 μm fluxes, we used zero-point fluxes of 645, 2408, and 3974 Jy for K, I, and B magnitudes, respectively. Filled circles with error bars indicate sources in the primary sample. Open circles indicate the supplementary sources. Color limits using 3 σ magnitude limits, or real measurements for saturated sources or for sources at the image boundaries, are indicated by arrows. Some sources are not shown because of lack of information, such as no data in the K band or no detections in both I and B bands. The concentration of galaxies at the upper left part of the panel is distinguished from the rest of the sample by more than the relatively large errors in the f_ν(6.7 μm)/f_ν (K) ratios. We assigned an identification flag of type I for galaxies in this concentration (Table 3). The type I galaxies are marked by squares and are separated from the rest of the galaxies by the dot-dashed line in the plot.

On the same panel, we overlaid some model predictions using the GRASIL SEDs (Appendix). The evolving SEDs for three $z = 0$ Hubble types—E, Sa, and Sc galaxies—are shown with dashed, dotted, and solid lines, respectively. For each Hubble type, we assumed three formation redshifts of z_f = 2, 3, and 10 (*thick, medium, and thin lines, respectively*). The locations of $z = 0$ galaxies are indicated by filled triangles, while $z = 1$, 2, and 3 are indicated by open triangles (for $z < z_f$). We find that type I galaxies follow lines for the evolving E galaxies at intermediate redshifts of $z = 0$–1, regardless of their assumed formation redshifts. The evolving Sa galaxy predictions also share the same region, but higher formation redshifts are preferred. In our adopted cosmology, the ages of galaxies with $z_f = 2$, 3, and 10 at $z = 1$ become 2.5, 3.6, and 5.3 Gyr, respectively. This indicates that type I galaxies are old and mature systems, whose stellar contents are already in place as a consequence of vigorous star formation that took place a long time ago (see Fig. 14).

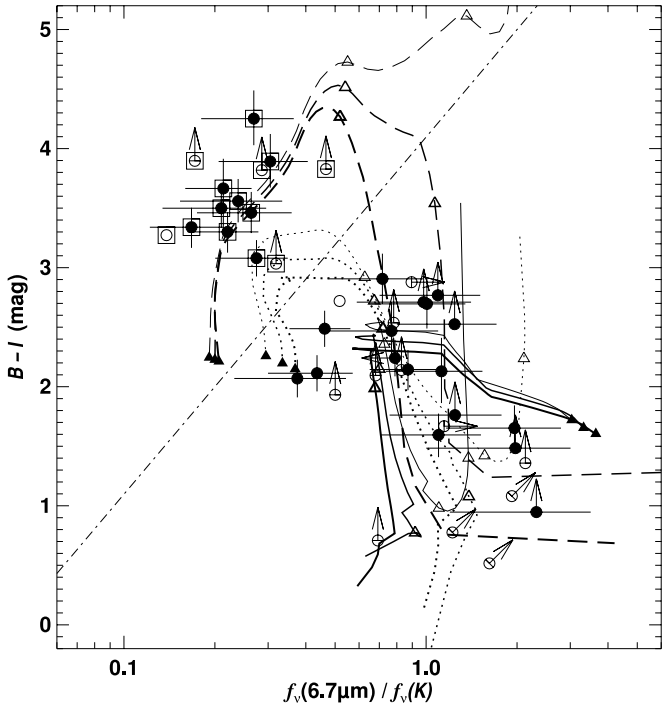

FIG. 2.—The f_ν(6.7 μm) /f_ν(K) vs. $B-I$ colors for the identified 6.7 μm galaxies. The sources in the primary (*filled circles*) and supplementary (*open circles*) samples (§ 2) are shown. The 1 σ error bars are marked only for the primary sources. For sources with enough information, the color limits are also indicated. We overlaid model predictions from the GRASIL SED library (see Appendix). Galaxies with star formation histories of the E (*dashed lines*), Sa (*dotted lines*), and Sc (*dash-dotted line*) types (Fig. 14) are shown. The assumed formation redshifts are z_f = 2 (*thick line*), 3 (*medium line*), and 10 (*thin line*). Triangles mark positions for $z = 0$, 1, 2, and 3 (for $z < z_f$; filled triangles for $z = 0$). In the upper left region of the plot separated by the dot-dashed line, i.e., $B-I > 3\log(f_\nu(6.7\ \mu\text{m})/f_\nu(K)/2) + 5$, we can identify a group of type I galaxies (*squares*). They are consistent with the evolving E galaxies at $z = 0$–1, or the Sa galaxies at $z = 0$–1 with high formation redshifts. It should be noted that the ages of galaxies with $z_f = 2$, 3, and 10 at $z = 1$ are 2.5, 3.6, and 5.3 Gyr, respectively, in our adopted cosmology. Thus, type I galaxies are mature systems with old stellar populations created by vigorous star formation episodes that took place a long time ago (see Fig. 14).

The other galaxies in this plot follow the GRASIL predictions; however, almost no conclusions can be drawn from this figure because of the degeneracy of the model loci. Both rapidly star-forming galaxies at high redshifts and quiescently star-forming galaxies show high ratios of $f_\nu(6.7\ \mu\mathrm{m})/f_\nu(K)$ and blue $B-I$ colors. The color degeneracy in this part of the plot can be disentangled to some degree by changing color combinations. In Figure 3, we show $f_\nu(6.7\ \mu\mathrm{m})/f_\nu(I)$ ratios and $B-K$ colors. In this plot, the evolving E or Sa galaxies can be red in both colors, while the evolving Sc galaxies occupy the lower left part of the panel with blue $B-K$ colors and low ratios of $f_\nu(6.7\ \mu\mathrm{m})/f_\nu(\mathrm{I})$. The evolving E and Sa galaxies with lower formation redshifts ($z_f < 3$) can have such blue colors at their forming stage ($z \sim z_f$). Thus, these blue colors can be an indicator of ongoing star formation.

The distribution of the 6.7 μm galaxies in this plot is rather smooth, except for the type I galaxies marked by squares. However, here we introduced a separation line (*dot-dashed line*) to extract many sources not detected in the B band. These can be explained as high-redshift galaxies ($z > 1$) with rapid star-forming activities in the past (evolving E or Sa galaxies). They represent post-starburst galaxies at high redshift. Their properties are consistent with those of ancestors of type I galaxies. Here we categorize them as type II and mark them with diamonds. The remaining galaxies are classified as type III. They are ongoing star formers at $z = 0$–2, a combination of mildly star-forming galaxies and vigorously star-forming galaxies with low formation redshifts.

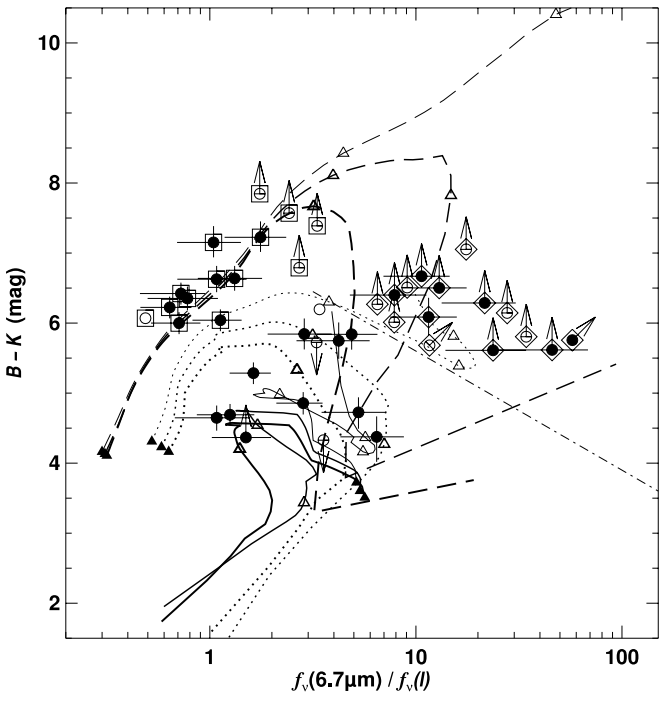

FIG. 3.—The $f_\nu(6.7\ \mu\mathrm{m})/f_\nu(I)$ vs. $B-K$ colors for the identified 6.7 μm galaxies. Symbols are the same as in Fig. 2, although plotted sources are slightly different because of the different color sets used. This diagram divides galaxies in the lower right region of Fig. 2 into two types. All the sources above the dot-dashed line, i.e., $B-K > -1.7\log[f_\nu(6.7\ \mu\mathrm{m})/f_\nu(I)] + 7.3$, which have red colors both in $f_\nu(6.7\ \mu\mathrm{m})/f_\nu(I)$ and $B-K$, are marked with diamonds (type II). The GRASIL SED predictions show that type II galaxies are $z > 1$ galaxies with intense star formation (evolving E or Sa galaxies). They are consistent with being ancestors of type I galaxies (*squares*). The remaining blue galaxies are categorized as type III. They have the colors of the evolving Sc galaxies or the E or Sa progenitors at $z \sim z_f$, suggesting ongoing star formation.

The division of the sources into types I, II, and III is made in color-color plots with photometry in all four bands—6.7 μm, K, I, and B. We find that this division can also be applied to the color-color plot of $f_\nu(6.7\ \mu\mathrm{m})/f_\nu(I)$ versus $f_\nu(6.7\ \mu\mathrm{m})/f_\nu(B)$. In this plot, we can assign type identifiers to all of the 6.7 μm sources, with the help of the distribution of the sources whose types have been defined in the two previous plots. Even unidentified sources could be nominally classified as type II, based on their red colors due to their flux limits in the I and B bands. For the primary sample, the number ratio for the 31 galaxies becomes type I:II:III = 11:10:10 including the unidentified source 27 with type II (Table 3). This almost even distribution skews toward the dominance of type II in the supplementary sample. For the 32 sources in this sample, the ratio becomes type I:II:III = 5:23:4. The dominance of type II in this fainter sample is still valid even if the seven unidentified sources assigned type II are excluded.

4.2. *Redshifts*

In order to obtain absolute quantities such as stellar masses for the 6.7 μm galaxies, we need their redshifts. For the 55 identified 6.7 μm galaxies, we do have 21 spectroscopic redshifts z_{sp}, of which 18 are for the primary sample (Songaila et al. 1994; Cowie et al. 1996; Barger et al. 2001). For others, we derived photometric redshifts z_{ph} in the following way.

4.2.1. *Photometric Redshifts*

Photometric redshifts were estimated by minimizing χ^2 values between photometric measurements and model estimates. This is basically the same method adopted in the HYPERZ code by Bolzonella, Miralles, & Pelló (2000). We used 6.7 μm, K-, I-, and B-band fluxes or their limits listed in Table 3. For sources in Table 2, we tried to utilize their flux values or their limits at the X-ray, submillimeter, and radio wavelengths as well. Model estimates were obtained using two sets of the star/dust SEDs in the GRASIL library, the evolving SEDs and the local ones (see Appendix). We also added two SEDs expanded to X-ray wavelengths; an NGC 6240 SED compiled by Hasinger (2000), and a GRASIL Arp220 SED complemented by X-ray and radio observations (Iwasawa 1999; Carilli & Yun 2000).

The χ^2 minimization was executed one by one for each SED in our code. The SEDs used have a long wavelength baseline; the GRASIL local SEDs from UV to submillimeter, the GRASIL evolving SEDs from UV to radio, and the two additional SEDs from X-ray to radio. They are likely to have significance variations at different wavelengths; however, we neglected such errors in the SEDs. We thus considered noise only in the absolute photometric measurements. For each SED, we calculated χ^2 values at 100 redshifts from $z = 0.1$ to 10. The interval of the redshift grid was constant in $\log(1+z)$. Once the redshift giving the minimum χ^2 value was derived, we repeated the calculation around this redshift with a 10 times finer redshift resolution. After completing the χ^2 minimization for all the SEDs, we determined a photometric redshift giving the minimum χ^2 value among the SEDs. We also found that, in most cases, the redshift giving the minimum χ^2 value for each SED is consistent with the photometric redshift determined by the global minimum in χ^2. It should be noted that the final photometric redshifts were all determined with the UV-to-submillimeter SEDs because the SEDs expanded to the radio and/or X-ray resulted in high χ^2 values. For the comparison of χ^2 values among SEDs with different wavelength spans, we took proper account of both

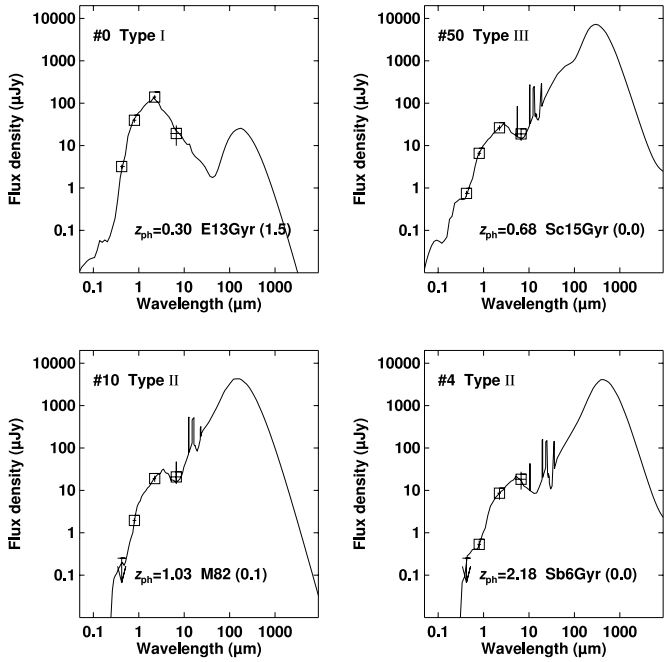

FIG. 4.—Some examples of the SED fits used to derive photometric redshifts. Detections are shown by squares in which flux errors and band widths are indicated by vertical and horizontal bars. Arrows are 3 σ upper limits. Source names and their photometric redshifts z_{ph} are given with their color types, GRASIL SED names, and χ^2 values (*in parentheses*).

the values of χ^2 and the number of detected data points used to calculate χ^2. In these calculations, we did not require that the age of the SED template be less than the age of the universe at a given redshift. Previous work on photometric redshifts have found good results with local templates at high redshifts (see, e.g., Hogg et al. 1998). We therefore tried to fit local SEDs even at $z = 10$. Old evolving SEDs were also treated as local SEDs. This assures a possible range of SED variations. Actually, we found that the results of this approach admitting the age-inconsistency in the fits gave the best results in the comparison with spectroscopic redshifts explained below.

We show some fitting results at different redshifts in Figure 4. Photometric redshifts and their 90% confidence limits (Avni 1976) are listed in Table 3. The names of the best-fit SEDs, their χ^2 values, and some ancillary information about the fits are also shown. It should be noted that many other SEDs gave quite similar redshift estimates with somewhat larger χ^2 values. For source 38, which has the largest χ^2-value in the sample, 12 SEDs gave $z = 0.74$–0.98 with $\chi^2 = 9.9$–15. On the other hand, many sources have $\chi^2 = 0.0$, though they are truncated values. This indicates overestimates of our photometric errors. In our case this is likely because of the quadratic summation of error components, each of which was difficult to determine independently. Our data points are very sparse in wavelength. In a sense, we might have used too many sets of SEDs for such data sets. It can be said that we have allowed the SEDs to shift freely in redshift space to take into account the symmetric distribution of photometric errors. We have succeeded in eliminating outlier fits; however, some fits could have fallen at rather artificial χ^2 minima. Thus, the confidence intervals are more reliable than the photometric redshift values themselves. It should be noted that the photometric redshift determination technique basically utilizes the characteristic spectral features common to all SEDs. There is some information in the fit; however, the very particular SED names identified as giving the best photometric redshifts do not exclude other SED types.

The reliability of these redshift estimates can be addressed by computing photometric redshifts for sources with spectroscopic redshifts. The results are shown in Figure 5. Of 21 sources with spectroscopic redshifts, 10 photometric redshifts were derived with the age-inconsistent evolving SEDs, six with local templates, and five with age-consistent SEDs. This result assures the usefulness of the allowing age-inconsistency in the fits. Actually, most of the photometric estimates distribute along the identity relation with their spectroscopic measurements. The nominal dispersion was 0.2 dex in $\log z$ (*dotted lines*). Only four sources, 62, 15, 29, and 16, with spectroscopic redshifts of $z \sim 0.2$, 0.3, 0.6, and 1.2, respectively, gave photometric redshifts more than 1 σ larger. However, their large 90% confidence intervals indicate that they are essentially problematic data sets. For example, source 62 lacks any flux constraint in the K band.

The four photometric bands, B, I, K, and 6.7 μm, are widely and evenly distributed in wavelength (Fig. 4). The determination of photometric redshifts with these data sets appears to depend on a characteristic spectral peak around 1.6 μm corresponding to the H^- opacity minimum for the stellar continuum emission. The use of this 1.6 μm bump for photometric redshifts with photometric data sets without wavelength gaps is described in Sawicki (2002). In wider wavelengths, the spectral slope is generally monotonic below 1.6 μm, while there could be UIB emission longward of the 1.6 μm peak until 6.7 μm (i.e., 3.3 and 6.2 μm). There is a possibility that some UIB emission was erroneously treated as a shorter wavelength feature. Misidentification of 6.2 μm emission with a 3.3 or 1.6 μm feature gives a wrong redshift

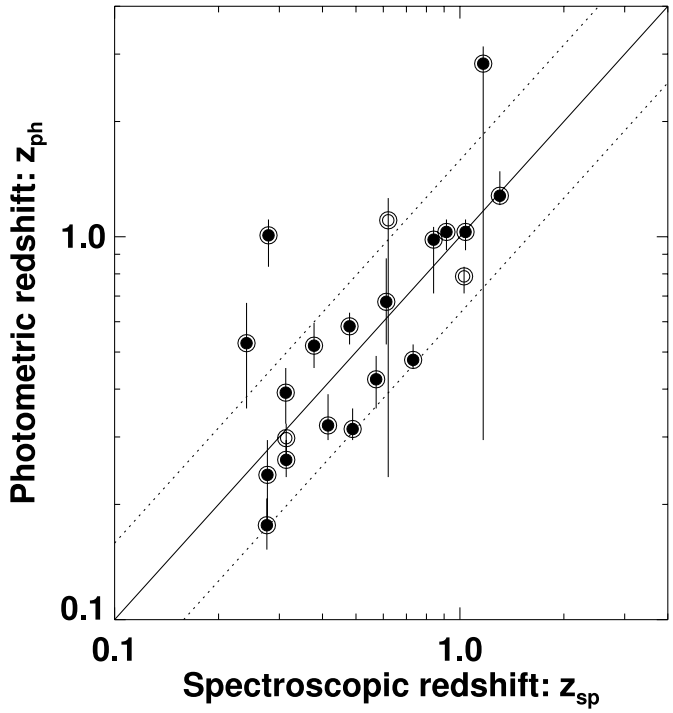

FIG. 5.—Comparison of photometric redshift estimates with spectroscopic redshift measurements. The filled and open symbols indicate the primary and supplementary sample galaxies (§ 2), respectively. The photometric redshifts were derived as in § 4.2.1 and their nominal 90% confidence limits are shown by vertical bars. Almost all the estimates are within a 1 σ range (0.2 dex; *dotted lines*) of the unity relation (*solid line*).

of $z \sim 1$ or 3 and that of 3.3 μm emission with a 1.6 μm feature gives $z \sim 1$. Unfortunately, the 6.7 μm photometric band is very broad (5–8.5 μm) and the gaps between the four photometric bands are somewhat large. Some sources are even lacking some of the four flux values. These factors could give a cause for the four high-redshift outliers in Figure 5. The effects of $z_{\rm ph} > z_{\rm sp}$ estimates will be addressed in the following sections.

4.2.2. *Fluxes and Redshifts*

With redshifts determined spectroscopically or photometrically, 6.7 μm fluxes for all 55 identified galaxies are plotted as a function of redshift in Figure 6. Flux errors are indicated with vertical bars, while horizontal bars are 90% confidence limits for photometric redshifts. Sources with spectroscopic redshifts are marked with double circles. Galaxies in the primary sample are marked with filled symbols.

For the primary sample, fainter galaxies tend to have higher redshifts. This usual trend seems to weaken below a flux level of 30 μJy, where high-redshift galaxies start to appear regardless of their flux values. This first finding is a direct result of the substantial depth of our imaging. Some photometric redshifts could be erroneously high (§ 4.2.1), but the high-redshift tail can be recognized even within the spectroscopic primary sample alone. There are some $z_{\rm sp} > 1$ galaxies with fluxes of $\sim$20 μJy. Most of the supplementary sample have $z_{\rm ph} > 1$. Because they are generally fainter than 30 μJy, this behavior itself strengthens the high-redshift tail seen in the primary sample. Two bright supplementary sources at $z \sim 2$ (12 and 34) are detected in relatively high-noise regions and lack K data. Thus, their significance is taken to be low.

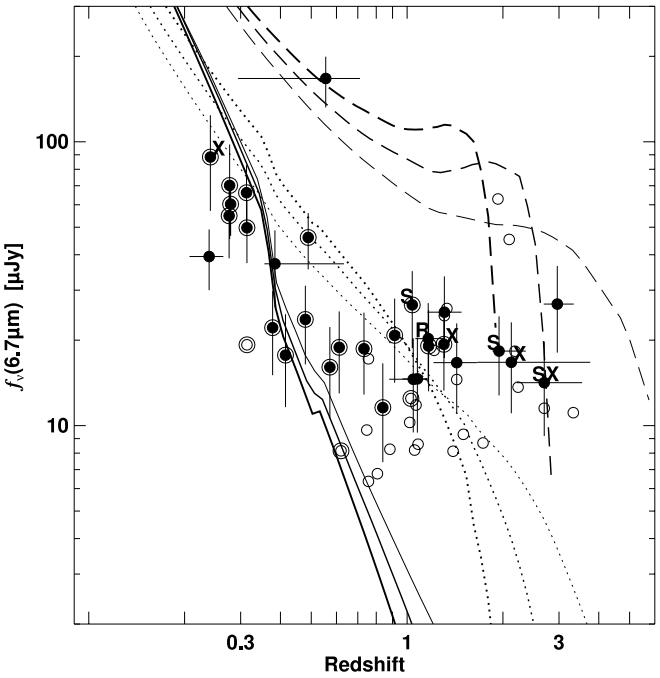

FIG. 6.—The 6.7 μm fluxes as a function of redshift. Sources with spectroscopic redshifts are indicated by double circles. The 90% confidence limits for photometric redshifts are indicated by horizontal bars. Vertical bars are 1 σ flux errors. Galaxies in the primary sample are shown by filled circles and the supplementary sources by open circles with no error bars. Letters, "X," "S," and "R" indicate the X-ray, submillimeter, and radio counterparts, respectively, listed in Table 2. Also shown are model predictions for the GRASIL evolving galaxies; E (*dashed lines*), Sa (*dotted lines*), and Sc (*solid lines*) (Appendix). For each SED, formation redshifts are assumed to be $z_f = 2$ (*thick line*), 3 (*medium line*), and 10 (*thin line*).

In this plot, model predictions are overlaid using the GRASIL library (see Appendix). Dashed, dotted, and solid lines are evolving E, Sa, and Sc galaxies and thick, medium, and thin lines are cases with formation redshifts of $z_f = 2$, 3, and 10, respectively. The distribution of the 6.7 μm galaxies is almost bracketed by these model predictions. At low redshifts ($z \sim 0.3$), most of the 6.7 μm galaxies are consistent with the evolving Sa and Sc galaxy models. The steep flux-redshift slopes for the evolving Sc galaxies are due to the effects of strong dust emission in the Sc galaxies to the 6.7 μm observing band. At high redshifts ($z \sim 1$), the distributions of both primary and supplementary galaxies are centered at model predictions for the evolving Sa galaxies. The flat flux-redshift distribution of the 6.7 μm galaxies at high redshifts can be reproduced well by a factor of a few less luminous versions of the evolving E galaxy models. Although the GRASIL models cannot be arbitrarily rescaled, especially at the UV and far-infrared wavelengths, where effects of dust are significant (Appendix), these model loci at $z > 1$ are primarily due to stellar emission in the rest-frame near-infrared, which accepts rescaling.

We mark the locations of the X-ray, submillimeter, and radio sources with letters, "X," "S", and "R," respectively. Except for one optically bright, hard X-ray source (62), all are within the high-redshift tail.

4.3. *Comparison with a $K < 20$ Sample*

Some of the characteristics of the faint 6.7 μm galaxies can be assessed in comparison with a K-band magnitude-limited sample. Here we utilize the $K < 20$ spectroscopic sample in the SSA13 field presented by Cowie et al. (1996). The field coverage of this K sample is a few times larger than that of the ISOCAM map.

First, we show a K-z diagram both for the 6.7 μm– and K-selected samples in Figure 7. Symbols are the same as in Figure 6, except $K > 20$ galaxies are overlaid as small squares. Note that some 6.7 μm galaxies plotted in Figure 6 are not shown here because they lack K photometry. The 6.7 μm galaxies with fainter K magnitudes tend to have larger redshifts. This feature is well described by the GRASIL evolving Sa galaxy model, and the distribution of the 6.7 μm galaxies in the plot lies between the evolving E and Sc galaxy predictions. No significant difference is seen between the primary and supplementary samples.

In contrast, the distribution of the K-band–selected galaxies extends to a region fainter than the evolving Sc galaxy model predictions and contrasts with the 6.7 μm sample. The 6.7 μm sample preferentially selects a high-redshift population at each K magnitude. At intermediate redshifts ($z = 0$–1), K-band emission is a good indicator of stellar mass (§ 5.1). The evolving Sc galaxy models at $z \sim 0.4$ have stellar masses of 0.1–0.2 $M^*_{\rm star}$, where we adopt $M^*_{\rm star} = 1.7 \times 10^{11}\ M_\odot$ (Cole et al. 2001). Thus, the $z < 1$ faint K galaxies should have very small stellar masses.

Next, we show I–K colors as a function of redshift in Figure 8. The 6.7 μm galaxies have red I–K colors especially at $z > 1$. This reddening trend is expected with the GRASIL models. However, some 6.7 μm galaxies exceed the red envelope of the GRASIL predictions. These excess red I–K colors are seen at intermediate redshifts for sources in the primary sample, and seem to be consistent with the presence of some high-redshift ($z > 1$) galaxies in the supplementary sample. The very red I–K colors at $z > 1$ indicate rapid star formation at very early epochs in the context of the GRASIL

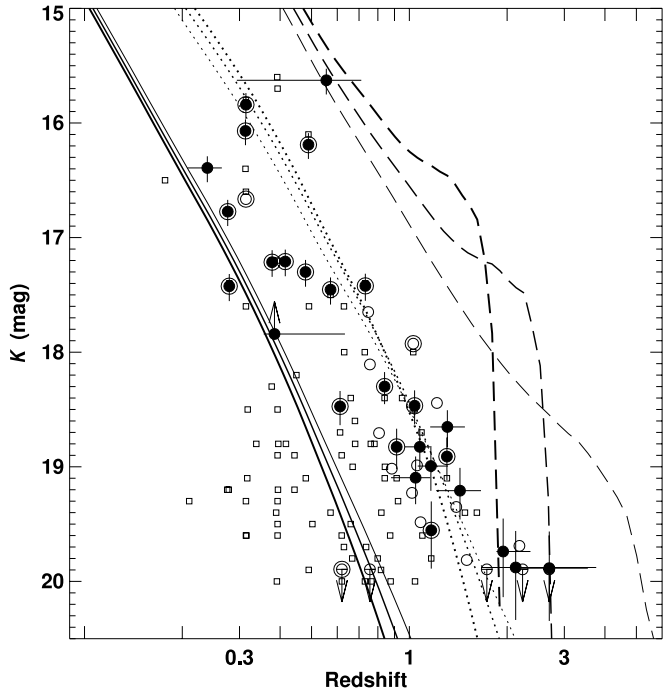

FIG. 7.—K magnitudes of the 6.7 μm galaxies. Symbols are the same as in Fig. 6. Some of the 6.7 μm sources are shown with their upper or lower magnitude limits, others are not shown because of they lack K photometry (Table 3). For reference, the figure is overlaid by a $K < 20$ spectroscopic sample (Cowie et al. 1996; *small squares*). The 6.7 μm–selected sample does not include faint K sources at low redshifts, some of which are even fainter than the GRASIL evolving Sc galaxy predictions.

model. The reddest $I-K$ colors in the 6.7 μm sample are comparable to those of an evolving E galaxy with a formation redshift of $z_f = 10$. For a brighter 6.7 μm sample, the existence of red $I-K$ sources is also reported in Flores et al. (1999a).

Most of the 6.7 μm galaxies have $I-K$ colors redder than the evolving Sc galaxy predictions. However, some K-band–selected galaxies have blue colors such as $I-K < 2$. Their blue colors imply that young stellar populations are dominant. As indicated with the GRASIL predictions at $z \sim z_f$, very blue $I-K$ colors can only be seen in the forming stages of galaxies. Thus, the blue K-selected galaxies should experience star-forming activities that are less burstlike than the evolving Sc galaxies, or they should start to form stars in a wide range of redshifts at $z = 0.3$–1.

We find that the K-band galaxies that are bluer than the evolving Sc galaxy predictions have K magnitudes that are fainter than the Sc galaxy models (Fig. 7). These K-selected galaxies having blue $I-K$ colors and faint K magnitudes at intermediate redshifts ($z < 1$) should have small stellar masses during their forming stages. Faint K-band–selected samples will be contaminated by this population of young dwarf galaxies at low redshifts. However, faint 6.7 μm–selected samples will be free from it, which means that an efficient search for high-redshift galaxies can be achieved with deep surveys at the mid-infrared, e.g., 6.7 μm.

5. STELLAR MASS

5.1. *Stellar Mass-to-Light Ratios*

For the conversion of observed luminosities to their stellar masses, we calculated stellar mass-to-light ratios at the observed bandpasses. These ratios are to be applied to the observed values directly. This approach is different from others in the literature (e.g., taking the observed K-band flux for a $z = 1$ galaxy, converting it to the rest-frame K band with an assumed SED, and applying a stellar mass-to-light ratio at the rest-frame K band). We eliminated the conversion to a fixed bandpass.

We calculated both stellar mass $M_{\rm star}$ and an in-band luminosity L that should be observed directly as a function of redshift. The in-band luminosities are presented in units of the bolometric luminosity of the Sun ($1\ L_{\odot,\rm bol} = 3.85 \times 10^{26}$ W). We adopted the evolving SEDs in the GRASIL library (see Appendix) and the resulting stellar mass-to-light ratios $M_{\rm star}/L$ are shown for the B, I, K, and ISOCAM LW2 bands (Fig. 9). Dashed, dotted, dot-dashed, and solid lines represent the evolving E, Sa, Sb, and Sc galaxies. Formation redshifts were assumed to be $z_f = 5$ and 10 (*thick and thin lines, respectively*).

It is well known that the rest-frame, K-band light is a good indicator of stellar mass. This fact is reflected in the K-band panel, showing very small dispersions among the cases for different galaxies or different formation redshifts, especially at low redshifts. At low redshifts, the dispersions among different models become larger at shorter wavelengths, here the I and B bands. The large dispersions at low redshifts in the 6.7 μm panel are due to contamination from dust emission.

Moving to larger redshifts, the dispersion among star-forming histories changes among the different observing bands. Very roughly, the effective wavelengths of the B, I, K, and LW2 bands are 2 times larger than those of the neighboring shorter bands. The dispersions for the I, K, and LW2 observing bands at $z \sim 1$ are very similar to those for the B, I, and K bands at $z \sim 0$. This means that 6.7 μm light is a better stellar mass indicator at high redshifts. On the other hand, B-band fluxes cannot be used to estimate stellar masses at high redshifts. They correspond to rest-frame UV fluxes, which are

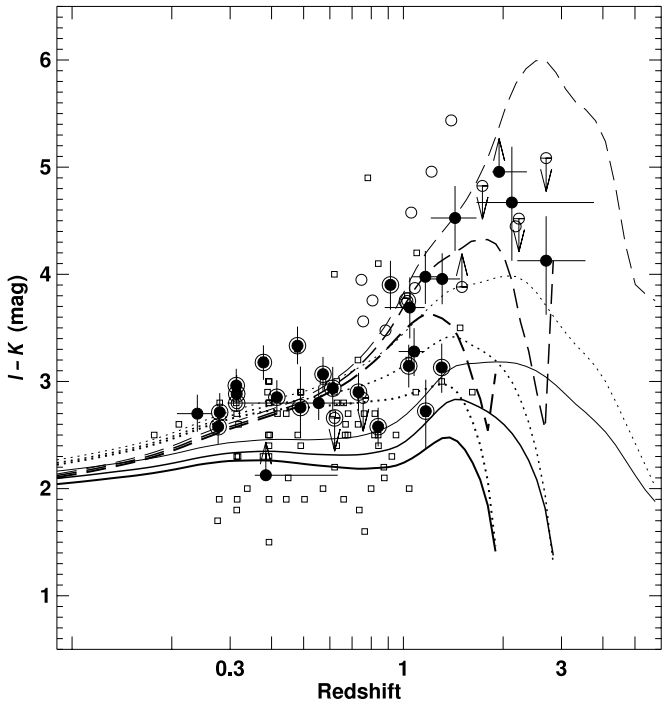

FIG. 8.—The $I-K$ colors of the 6.7 μm galaxies. Symbols are the same as in Fig. 7. The 6.7 μm–selected sample does not include blue $I-K$ sources at low redshifts, some of which are even bluer than the GRASIL evolving Sc galaxy predictions.

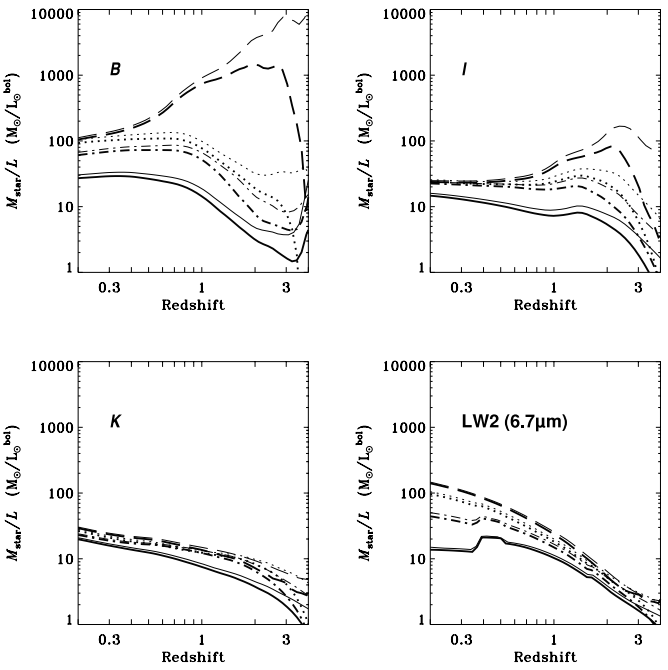

FIG. 9.—Stellar mass-to-light ratios as a function of redshift. They are estimated for observations at the *B*, *I*, *K*, and ISOCAM LW2 (6.7 μm) bands. The in-band luminosity at each observing band corresponds to different wavelengths with increasing redshift. Thus, for the calculation of the ratios, we adopt luminosities in units of the bolometric luminosity of the Sun ($1\ L_{\odot,\mathrm{bol}} = 3.85 \times 10^{26}$ W). Lines show the GRASIL models for the evolving E (*dashed lines*), Sa (*dotted lines*), Sb (*dot-dashed lines*), and Sc (*solid lines*) galaxies are shown. Two formation redshifts are assumed; $z_f = 5$ (*thick line*) and 10 (*thin lines*).

good indicators of star formation rates. Emission at short wavelengths such as UV emission is sensitive to ages of galaxies, or formation redshifts. Such effects are actually seen in the *B*-band panel. They can also be seen in the *K*-band panel at high redshifts.

5.2. *Stellar Masses of Faint 6.7 μm Galaxies*

The stellar masses of the faint 6.7 μm galaxies were derived from rest-frame near-infrared light taking into account the behavior of the stellar mass-to-light ratios in Figure 9; the conversion of luminosities to stellar masses was performed using 6.7 μm luminosities for sources at $z > 1$ and *K*-band luminosities for sources at $z < 1$. For low-redshift galaxies with no *K* photometry, we used *I*-band luminosities instead. This approach minimized the uncertainties in stellar mass-to-light ratios. In addition, we determined the SEDs used to derive stellar mass-to-light ratios by fitting all the photometry data from UV to submillimeter via χ^2 minimization to the evolving SEDs in the GRASIL library (see Appendix). Because older SEDs usually have higher stellar mass-to-light ratios, we set an age constraint for the fitting template. No SEDs older than the age of the universe at the source's redshift were used for the fitting. This avoids artificially high estimates of stellar mass-to-light ratios at the expense of increasing the nominal χ^2 of the best fit. Note that χ^2 values for sources with spectroscopic redshifts can be larger than those for sources with photometric redshifts. This is because some fraction of inappropriateness of the model SEDs is absorbed in the fits in determining photometric redshifts. However, such errors are reflected in the uncertainties of the photometric redshifts.

The resulting stellar masses using the best-fit stellar mass-to-light ratios are listed in Table 3. The names of the SEDs used, their χ^2 values, and some ancillary information of the fitting are also shown. In order to derive errors in stellar mass-to-light ratios, we searched SED fits with $\Delta\chi^2 = 1$ from the best-fit SED (Avni 1976). For some sources, no such SED fits were found to determine confidence limits because of the sparse grid of SEDs. In such cases, we adopted stellar mass-to-light ratios of the SED fits with the minimum $\Delta\chi^2$ values. Even with such overestimated noise, we found that the photometric errors dominate the total uncertainties in the stellar masses. This is because any effects on the stellar mass-to-light ratio values were minimized as a result of our hybrid conversions using 6.7 μm and *K*-band luminosities. The actual trend can be seen in Figure 10. Larger errors in stellar masses for sources at $z > 1$ originate in larger photometric errors in their 6.7 μm fluxes. We also note that our stellar mass estimates are not likely to be affected by the limitation of rescaling in the GRASIL SED model because the rest-frame near-infrared light is negligibly affected by dust (see Appendix).

Many 6.7 μm galaxies have stellar masses as massive as $10^{11}\ M_\odot$. The characteristic stellar mass of local galaxies, $M^*_{\mathrm{star}} = 1.7 \times 10^{11}\ M_\odot$ (Cole et al. 2001), is indicated by a horizontal dot-dashed line. Also shown are stellar masses of the evolving E galaxy (*dashed line*) with a formation redshift of $z_f = 10$ scaled to the minimum 6.7 μm flux of the primary sample (12 μJy). This shows that M^*_{star} galaxies could be

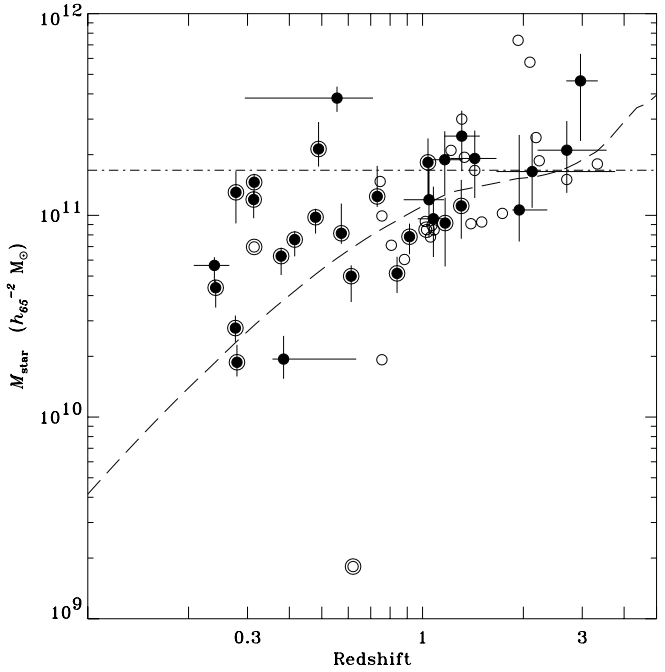

FIG. 10.—Stellar masses of the 6.7 μm galaxies. Symbols are the same as Fig. 6. The stellar masses are derived from 6.7 μm luminosities at $z > 1$ or *K*-band luminosities otherwise. If no *K*-band luminosities are available, *I*-band luminosities are used instead. Note that errors in stellar mass come mainly from errors in photometry, not from errors in stellar mass-to-light ratios derived from the SED fit. A horizontal dot-dashed line indicates the characteristic stellar mass of local galaxies (Cole et al. 2001). A dashed line shows stellar mass predictions assuming the GRASIL evolving E galaxy with a formation redshift of $z_f = 10$. They are scaled to the minimum 6.7 μm flux of the primary sample (12 μJy). This curve itself is useful to indicate the redshift dependence of the detection limit especially at the high-redshift end where the scaling from the GRASIL model is almost unity. However, the scaling factor becomes very small, ~0.03 (0.1 M^*_{star}) at $z = 0.2$ (see Appendix). So, the uncertainties of the dashed line at low redshift will be large. Moreover, 6.7 μm fluxes start to be affected by dust emission at such low redshifts. Note that stellar masses were derived from *K* fluxes at $z < 1$.

detected out to $z \sim 3$, if such galaxies were present. Some 6.7 μm sources have stellar masses smaller than this GRASIL prediction. They are likely to have star formation histories that are less burstlike than the evolving E galaxy or lower formation redshifts of $z_f < 10$. This curve itself is useful in indicating the redshift dependence of the detection limit, especially at the high-redshift end where the scaling from the GRASIL model is almost unity. However, the scaling factor becomes very small, $\sim$0.03 (0.1 $M^*_{\rm star}$), at $z = 0.2$ (see Appendix). So, the uncertainties of the dashed line at low redshift will be large. Moreover, 6.7 μm fluxes start to be affected by dust emission at such low redshifts. Note that stellar masses were derived from K fluxes at $z < 1$.

The distribution of the supplementary sample is similar to that of the primary sample. Two of the highest stellar mass sources in the supplementary sample at $z \sim 2$ (sources 12 and 34) are the dubious sources mentioned in § 4.2.2. The lowest stellar mass for the supplementary sample at $z \sim 0.6$ (source 29) falls somewhat far from the distribution of other sources. This is derived from its I-band luminosity and could be somewhat less secure.

5.3. *Epoch-dependent Stellar Mass Functions*

Here we examine the redshift dependence of the stellar mass function. The epoch-dependent stellar mass functions $\Phi(M_{\rm star}, z)$ were estimated with the $1/V_{\rm max}$ method (e.g., Takeuchi, Yoshikawa, & Ishii 2000) as

$$\Phi(M_{\rm star}, z) = \sum \frac{1}{V_{\rm max}}. \quad (3)$$

No sources in the supplementary sample were used in the summation in order to avoid the unwanted effects of spurious detections (§ 2). Taking into account errors in photometric redshifts, we adopted three broad redshift bins; $z = 0.2$–0.5, 0.5–1.2, and 1.2–3.0. The widths of these bins are almost 0.4 dex in $\log z$. The maximum volume $V_{\rm max}$ for each source was derived according to

$$V_{\rm max} = \int_{z_{\rm min}}^{z_{\rm max}} \Omega(<S(z)) \frac{d^2V}{d\Omega dz}\, dz, \quad (4)$$

where $\Omega(<S)$ is the effective solid angle in this survey for a source with a flux S. This function is presented in Sato et al. (2003). The flux of a source at a redshift z is $S(z)$ derived using the best-fit SED for the stellar mass. The comoving volume element $d^2V/d\Omega\, dz$ is calculated with formulae from Carroll, Press, & Turner (1992) and Hogg (1999). The redshift integration range is determined by the criteria of the primary sample. The value of $z_{\rm max}$ is the smaller of (1) the redshift at which the source has the minimum S/N in the primary sample, or (2) the upper end of the redshift bin. The value of $z_{\rm min}$ is the larger of (1) the redshift at which the source exceeds the maximum flux in the primary sample, or (2) the lower end of the redshift bin.

We computed stellar mass functions both for the spectroscopic sample and for the combined sample of galaxies with spectroscopic and photometric redshifts (Table 4). Stellar mass functions for the spectroscopic sample are listed to indicate the strict lower limits. The 1 σ errors are also shown, estimated from Poisson statistics and uncertainties in $V_{\rm max}$. The numbers in parentheses are the number of galaxies that were used in the calculation. Because of the small sample size, we only used four broad stellar mass bins. Some values are missing because of the limited survey volume (at the high stellar mass end at low redshift) and limited sensitivity (at the low stellar mass end at high redshift). With such restrictions, there are few overlaps among the redshift bins for a fixed stellar mass bin. In each of such overlapping stellar mass bin, we find that comoving space densities are decreasing with redshift. For a stellar mass range for typical local galaxies $\{\log[M_{\rm star}(h_{65}^{-2}\, M_\odot)] = 10.95$–$11.35\}$, the comoving space density at $z = 1.2$–3.0 becomes 10% (-1.0 dex) of that at $z = 0.2$–0.5.

These stellar mass function estimates are compared with local ones in Figure 11. Cole et al. (2001) derived a local stellar mass function with a large sample of matched 2 Micron All Sky Survey (2MASS)-Two Degree Field Galaxy Redshift Survey (2dFGRS) galaxies. Their stepwise maximum likelihood estimates are shown with diamonds in the upper left panel. The assumed initial mass function (IMF) was a Salpeter-type (Salpeter 1955). The error bars are also shown. The minimum error is obtained at almost a characteristic stellar mass of $M^*_{\rm star} = 1.7 \times 10^{11}\ M_\odot$, which is converted to our cosmology. The redshift distribution of the 2MASS-2dFGRS

TABLE 4

Stellar Mass Functions and Stellar Mass Densities

z Range	$\log \Phi(M_{\rm star}, z)$ (h_{65}^3 Mpc^{-3} dex^{-1})				$\log \rho_{\rm star}(z)$ ($h_{65}\, M_\odot$ Mpc^{-3})
	10.15–10.55	10.55–10.95	10.95–11.35	11.35–11.75	
Combined Sample					
0.2–0.5	$-2.3^{+0.5}_{-0.5}$ (3)	$-2.2^{+0.3}_{-0.4}$ (4)	$-2.3^{+0.3}_{-0.3}$ (5)	...	$8.7^{+0.2}_{-0.2}$ (12)
0.5–1.2	...	$-2.5^{+0.5}_{-0.6}$ (4)	$-2.9^{+0.3}_{-0.3}$ (6)	$-3.8^{+0.7}_{-1.0}$ (1)	$8.2^{+0.3}_{-0.3}$ (11)
1.2–3.0	...	...	$-3.3^{+0.4}_{-0.5}$ (5)	$-4.0^{+0.5}_{-0.7}$ (2)	$7.6^{+0.3}_{-0.4}$ (7)
Spectroscopic Sample					
0.2–0.5	$-2.5^{+0.4}_{-0.6}$ (2)	$-2.4^{+0.3}_{-0.5}$ (3)	$-2.3^{+0.3}_{-0.3}$ (5)	...	$8.6^{+0.2}_{-0.3}$ (10)
0.5–1.2	...	$-2.5^{+0.5}_{-0.6}$ (4)	$-3.2^{+0.4}_{-0.5}$ (3)	...	$8.1^{+0.4}_{-0.4}$ (7)
1.2–3.0	...	...	$-3.7^{+0.9}_{-1.4}$ (1)	...	$6.9^{+0.9}_{-1.5}$ (1)

Notes.—Epoch-dependent stellar mass functions $\Phi(M_{\rm star}, z)$ for the listed ranges of $\log M_{\rm star}$ ($h_{65}^{-2}\ M_\odot$) and stellar mass densities $\rho_{\rm star}(z)$ are derived from the 6.7 μm primary sample. Two sets of estimates are obtained; one with the combined (photometric and spectroscopic) sample and the other with the spectroscopic sample. The 1 σ errors are estimated from uncertainties in $V_{\rm max}$ and Poisson statistics. For stellar mass densities, errors in stellar mass are also taken into account. Numbers in parentheses are the number of 6.7 μm galaxies used in the calculation.

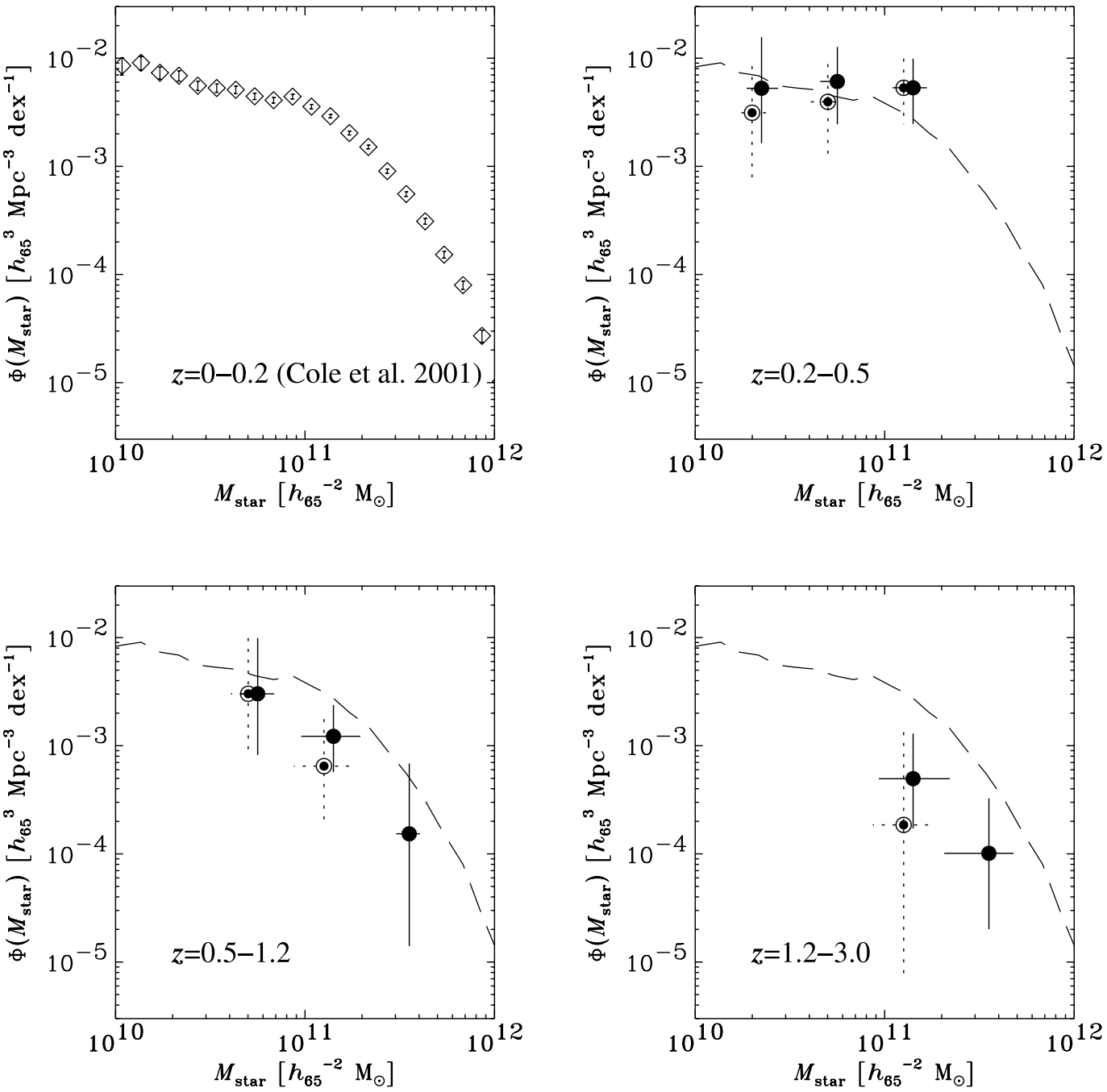

FIG. 11.—Stellar mass functions at four epochs. For a local stellar mass function, the stepwise maximum likelihood estimates for a Salpeter IMF are reproduced from Cole et al. (2001). The accompanying errors are plotted, though almost all are within symbols for values (*diamonds*). This local stellar mass function is reproduced in three higher redshift panels (*dashed lines*). In each of these panels, our stellar mass function estimates are shown for the combined (photometric and spectroscopic; *filled circles*) and for the spectroscopic (*double circles*) samples. The double circles are shifted slightly. Vertical errors are uncertainties in V_{max} and Poisson statistics. Horizontal errors are mean fractional errors in stellar mass.

galaxies is largely confined to $z = 0$–0.2 with a peak around $z = 0.05$. This local stellar mass function is represented by dashed lines in higher redshift panels for comparison with our estimates. Filled and double circles show our stellar mass functions derived with the combined and spectroscopic samples, respectively. The values for the spectroscopic sample are shifted leftward by 0.05 dex. Vertical error bars come from Table 4. Horizontal error bars are mean fractional errors in stellar masses.

In the $z = 0.2$–0.5 bin, our stellar mass function estimates are consistent with the local ones within 1 σ. At higher redshifts, stellar mass functions estimated with 6.7 μm galaxies start to show lower values than the local ones. At redshifts of $z = 0.5$–1.2, the deviations are somewhat marginal. The deviations appear to be larger at larger stellar masses. At the highest redshift bin $z = 1.2$–3.0, the deviations from the local sample are more than 1 σ. These deviations could be much larger if we took into account our tendency to overestimate photometric redshifts (§ 4.2.1). Cosmological surface brightness dimming could result in a smaller number of galaxies at high redshifts. However, our sample has been selected from a 6.7 μm map with a broad beam,

corresponding to a very deep surface brightness sensitivity (0.02 μJy arcsec^{-2} at 1 σ).

The decrease in the comoving space density of massive stellar systems at high redshifts has also been seen in *K*-band–selected data by Drory et al. (2001). They presented integrated stellar mass functions above three mass thresholds (Fig. 12), which are almost comparable to our largest three mass bins (Table 4). Their integrated stellar mass functions (*squares*) for $\log[M_{\rm star}(h_{65}^{-2}\ M_\odot)] > 11.07$ and $\log[M_{\rm star}(h_{65}^{-2}\ M_\odot)] > 11.37$ show declines of -0.5 and -0.8 dex from $z = 0.5$ to 1.1. Our integrated stellar mass functions (*circles*) have a good consistency in the overlapping redshift range. For the lowest mass threshold panel, our highest redshift bin values are lower limits, because of limited sensitivity (Table 4). Note that Drory et al. (2001) adopted the maximum mass-to-light ratios assuming the age of the universe. The local values using the stellar mass function of Cole et al. (2001) are marked as references (*diamonds*). Our values at $z = 0.3$ are somewhat larger than those of Cole et al. This difference may result from cosmic variance, because our surveyed volume at such low redshift is much smaller than that of Cole et al.

5.4. *Stellar Mass Density in the Universe*

Using the stellar mass estimates for the 6.7 μm galaxies, we derived their contributions to the stellar mass density in the universe. Epoch-dependent stellar mass densities $\rho_{\rm star}(z)$ are obtained as

$$\rho_{\rm star}(z) = \sum \frac{M_{\rm star}}{V_{\rm max}}, \qquad (5)$$

utilizing the $V_{\rm max}$ values calculated in § 5.3. Here again, we used only the primary sample for the summation. Our derived stellar mass densities for the three redshift bins are direct sums. Our stellar mass function estimates have narrow mass ranges and large errors (Fig. 11). They could not be used to derive characteristic masses and low-mass slopes, which are needed to properly integrate stellar mass functions over the full mass range. Thus, we decided to use direct sums in order to avoid large uncertainties in corrections to fully integrated values. Our directly summed stellar mass densities are shown in Table 4. Their errors are estimated from Poisson noise and uncertainties in stellar mass and $V_{\rm max}$. The numbers of sources used in each summation are indicated in parentheses. Stellar mass density becomes smaller at higher redshifts. It should be noted that the 6.7 μm galaxies that contribute these values come from different stellar mass ranges, as indicated in the left columns.

The contributions of our 6.7 μm galaxies to the stellar mass density in the universe are shown as a function of redshift in Figure 13. Filled and double circles were estimated from the combined and spectroscopic samples, respectively. Double circles are shifted slightly to lower redshifts. Horizontal bars show bin widths and vertical bars mark 1 σ uncertainties. We overlaid several stellar mass densities from the literature as triangles (Giallongo et al. 1998), open circles (Brinchmann & Ellis 2000), a diamond (Cole et al. 2001), crosses (Cohen 2002), open squares (Dickinson et al. 2003), and filled squares (Fontana et al. 2003).

The local value by Cole et al. (2001) was obtained from their stellar mass function, which is deduced assuming a Salpeter IMF. The value is derived for the full mass range by integrating the Schechter fit to the stellar mass function. Dickinson et al. (2003) also adopted fully integrated values over the full mass range. They first derived luminosity densities by integrating the Schechter fit to their rest-frame *B*-band luminosity function at each redshift and then converted them with their mean *B*-band mass-to-light ratio into stellar mass densities. Fontana et al. (2003) followed this method. Cohen (2002) used the integration of the Schechter fits to her *K*-band luminosity functions, but for a restricted range from $10L^*$ to $1/20L^*$. These quasi-integrated values were converted with a fixed $z = 0$ stellar mass-to-light ratio of $M_{\rm star}/L_K = 0.8$ in solar units. Note that this $M_{\rm star}/L_K$ ratio has a different meaning from our $M_{\rm star}/L$ ratio for the *K* band in units normalized to the bolometric solar luminosity (§ 5.1), which is shown in Figure 9. Brinchmann & Ellis (2000) also adopted the value of $M_{\rm star}/L_K = 0.8$ to derive incompleteness corrections. Their values are quasi-full integrations for a limited mass range of $10.5 < \log[M_{\rm star}(h_{65}^{-2}\ M_\odot)] < 11.6$ (cf. Table 4). The values from Giallongo et al. (1998) are direct sums for $20 < R' < 25$ galaxies around a $z = 4.7$ quasar. Their values are multiplied by 2 to take account of their adopted Miller-Scalo IMF.

Some authors assumed a Schechter form; however, the shape of stellar mass functions is not yet determined (cf.

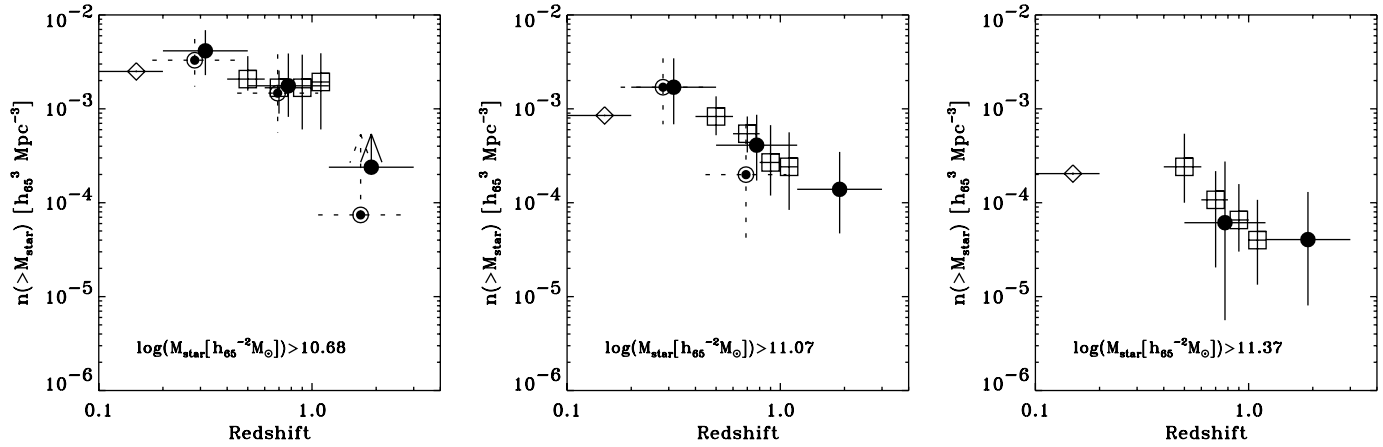

FIG. 12.—Redshift dependence of integrated stellar mass functions. Lower stellar mass thresholds are those in Drory et al. (2001). Our estimates are shown as in Fig. 11. Values from Drory et al. (2001) are represented as squares with vertical error bars indicating their field-to-field fluctuations. Diamonds show local values calculated from a stellar mass function by Cole et al. (2001).

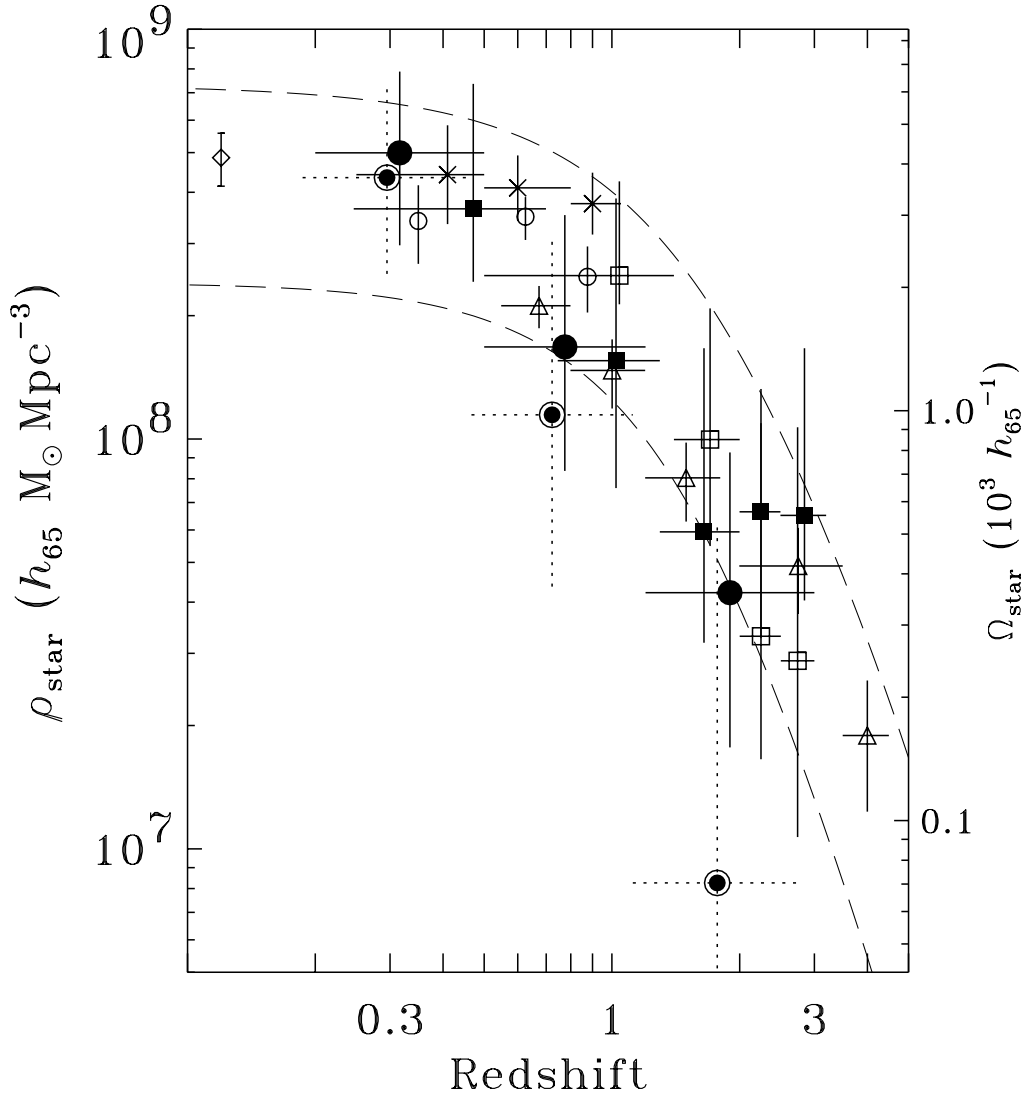

FIG. 13.—Stellar mass density in the universe as a function of redshift. The right axis shows densities normalized to the critical density of the universe. The contributions of the 6.7 μm galaxies are shown for the combined (*filled circles*) and spectroscopic (*double circles*) samples. The double circles are plotted at slightly lower redshifts. The horizontal bars represent the redshift ranges of the bins and the vertical bars show 1 σ errors, taking account of Poisson noise and uncertainties in stellar mass and $V_{\rm max}$. Several other estimates are overlaid; a *K*-band–selected sample with photometric redshifts (Fontana et al. 2003; *filled squares*), an *H*-band–selected sample with photometric redshifts (Dickinson et al. 2003; *open squares*), a *J*-band–selected spectroscopic sample (Cole et al. 2001; *diamond*), an *I*-band–selected spectroscopic sample (Brinchmann & Ellis 2000; *open circles*), an *R*-band–selected spectroscopic sample (Cohen 2002; *crosses*), and an R'-band–selected photometric sample around a $z = 4.7$ quasar (Giallongo et al. 1998; *triangles*). The open and filled squares and the diamond are obtained from full integration of a Schechter fit to their respective luminosity or stellar mass function at each redshift bin. The crosses and the open circles are quasi-fully integrated values with a finite integration range from $10L^*$ to $1/20L^*$, and $10.5 < \log [M_{\rm star}(h_{65}^{-2}\ M_\odot)] < 11.6$, respectively. The triangles are simply summed values of the detected sources like ours. We adopted the mean redshifts of Cohen (2002) and all four cases discussed in Dickinson et al. (2003) for their error bars. Miller-Scalo IMFs were used in Giallongo et al. (1998). All points plotted here were normalized to our cosmology and a Salpeter IMF with mass limits of 0.1 and 125 $M_\odot$. The two dashed curves are deduced by integrating the star formation rate density in the universe, which is derived from the UV luminosity density as a function of redshift (Cole et al. 2001). The upper curve is an extinction-corrected case for $E(B-V) = 0.15$, and the lower one has no dust correction.

Salucci & Persic 1999). We therefore did not apply any corrections to these values derived for the different mass ranges. We made crude corrections only for the different cosmologies. Although the reported values are basically binned values, we took each of them as a single representative value at each redshift with a fixed redshift range. For correcting the values of Cohen (2000), we took her mean z values as their representative redshifts. For Brinchmann & Ellis (2000), we adopted midpoints in $\log z$ calculated with their bin boundaries. We did not consider effects from sources near the boundaries of the bins or with different $z_{\rm min}$ and $z_{\rm max}$ values.

At lower redshifts ($z < 0.5$), almost all the estimates are consistent and very near to the local value. This suggests that the surveys cited here have succeeded in detecting most of the stellar mass in galaxies at these redshifts. At a higher redshift ($z \sim 1$), differences between the results become somewhat larger. The use of a fixed stellar mass-to-light ratio of $M_{\rm star}/L_K = 0.8$ in Cohen (2002) and Brinchmann & Ellis (2000) could explain some of the values in excess of ours at $z \sim 1$. According to Drory et al. (2001), stellar mass-to-light ratio $M_{\rm star}/L_K$ is a decreasing function of redshift: 0.99, 0.88, 0.73, and 0.65 for $z = 0.5$, 0.7, 0.9, and 1.1, respectively. They assumed the maximum ages for the passively evolving galaxies; thus, the decline in $M_{\rm star}/L_K$ could be steeper. Note that the decline in the $M_{\rm star}/L$ ratios at the *K* band in Figure 9 come from the evolution of the galaxies but also from the effects of

the shifting observing band. Direct sums of only the detected sources are likely to miss low-mass galaxies below the detection limits. Therefore, our spectroscopic points, which are derived from our subsamples, should be regarded as strict lower limits. At even higher redshifts ($z \sim 2-3$), the values from Giallongo et al. (1998) appear to have a milder decline, especially compared with those of Dickinson et al. (2003). This might be related to their use of the different IMF in the estimation. However, Fontana et al. (2003) presented high stellar mass densities at these redshifts. This suggests that we need to survey a much larger area to determine the true stellar mass densities at high redshift.

The evolution of stellar mass density is related to that of the star formation rate density in the universe. Star formation rate indicators at UV wavelengths are sensitive to dust extinction. Cole et al. (2001) adopted two cases; $E(B-V) = 0$ and $E(B-V) = 0.15$. For each case, they provided an analytic formula fitted to the UV observations of the star formation rate density. By integrating these formulae with time, we estimated the evolution of stellar mass density in the universe. Here the recycling fraction of stellar mass for the next generation stars was assumed to be $R = 0.28$ for a Salpeter IMF. The results are overlaid as dashed lines in Figure 13. Lower and upper lines correspond to the $E(B-V) = 0$ and $E(B-V) = 0.15$ cases, respectively. It should be noted that these lines are shown with units of $M_{\odot}$ Mpc^{-3} with no dependence on the Hubble parameter because of the cancellation in the time integration.

These time-integrated values of the star formation rate densities are derived by the integration of the full range of star formation rate or luminosity at each epoch. When we assume $E(B-V) = 0.15$, the line calculated from the time integration of the star formation rate densities is always higher than any of the stellar mass density points estimated for the full or the quasi-full range of stellar mass. This might suggest that the mean dust extinction value would be lower than $E(B-V) = 0.15$. In fact, a median $E(B-V)$ value for the $z \sim 4$ Lyman break galaxies is somewhat lower than $E(B-V) = 0.15$ (Steidel et al. 1999). However, it should be noted that all the full or quasi-full integrated values for the stellar mass densities at high redshifts were derived from the rest-frame UV or optical light only. In addition to the underestimation of this light due to a certain level of dust extinction, there remains some possibility that highly reddened systems were completely neglected because of their nondetection. In fact, a star formation rate density estimate comparable to the values for the case of $E(B-V) = 0.15$ was obtained with only a few submillimeter sources (Hughes et al. 1998). No contributions from such dusty galaxies were taken into account in the Cole et al. (2001) formulae. It should be noted that our stellar mass density estimates include contributions from the three submillimeter galaxies in this field. At 6.7 μm, we can probe the rest-frame near-infrared light out to quite a high redshift. Because dust extinction at the rest-frame near-infrared is almost negligible, underestimates of stellar mass densities are unlikely to happen either because of loss of light or by nondetections.

6. DISCUSSION

The contributions of the faint 6.7 μm galaxies to the stellar mass density in the universe are estimated to be comparable to those inferred from observations of UV-bright galaxies. Unfortunately, 6.7 μm observations probe a narrow mass range and UV observations suffer from dust effects, preventing us from making detailed comparisons between the two.

On the other hand, we found that the faint 6.7 μm galaxies generally had red colors. A comparison with a particular population synthesis model suggests that they have experienced vigorous star formation at high redshifts. The derived large stellar masses for the faint 6.7 μm galaxies also support such star-forming events in the past. Beyond the redshift range of our sample ($z > 3$), we know that there exist Lyman break galaxies. They are blue and forming stars; however, their masses are generally smaller than the masses of this faint 6.7 μm sample. In a naive sense, several Lyman break galaxies must merge to form a massive 6.7 μm galaxy. Or, very rapid star-forming systems are needed. SCUBA galaxies are expected to have such efficient star-forming activities. However, at least in this field, SCUBA sources were already identified as faint 6.7 μm galaxies at relatively small redshifts.

We noticed the existence of massive galaxies out to $z = 3$. At the same time, their comoving space densities were found to be lower than the present values. Thus, there should be some mass assembly activities to build up massive galaxies in a redshift range of $z = 0$–3. They should be forming stars in situ, merging, or a combination of the two. The investigation of such build-ups in $z = 0$–3 would give us important insights into the build-ups in the higher redshift regime. A large number of star-forming galaxies detected at 15 μm with *ISO* may give an unbiased sample for this purpose because of their insensitivity to dust.

The detection of all the X-ray, submillimeter, and radio sources in this field at 6.7 μm is interesting. Most of our knowledge of the evolution of galaxies has been based on investigation of stellar systems, such as optical observations of UV emission from massive stars. However, a higher fraction of active galaxies detectable at other wavelengths in the distant universe requires the consistent understanding of the evolution of multiple components in galaxies. Far-infrared/submillimeter observations of dust and X-ray/radio observations of active galactic nuclei (AGNs) might provide us with more essential information than UV/optical/near-infrared observations for stellar components.

We have stated that mid-infrared observations resulted in an investigation of a narrow range of stellar masses. We regard this as a good property, i.e., allowing the preparation of a mass-ordered sample to compare stars/dust/AGNs with multiwavelength observations. With mid-infrared surveys in the near future, we expect to construct well-controlled samples of distant galaxies.

7. CONCLUSIONS

The tight correlation between the stellar masses of galaxies and their rest-frame near-infrared luminosities can be a strong tool for investigating the evolution of stellar mass assembly in galaxies. The effect of redshift has motivated us to observe high-redshift galaxies in the mid-infrared. The mid-infrared sources detected in the SSA13 field with the ISOCAM LW2 (6.7 μm) filter are identified, and their nature and stellar masses are discussed. The 65 sources are divided into two subsamples, a primary sample of 33 sources (of which two are stars) and a supplementary sample of 32 sources. No spurious sources are expected in the primary sample. Taking into account the higher source densities at the optical and near-infrared, the identifications at these wavelengths were determined using two possibilities; a true association and a chance event. Using the highest ratio of the two, 32 out of the 33 primary sources and 25 out of the 32 supplementary sources were identified. A test of the identification procedure with the

negative sample showed that for the supplementary sample, identifications at the K band should be secure, while a few identifications at the I band might be wrong. A comparison with the published X-ray, submillimeter, and radio catalogs resulted in mid-infrared identifications of all (four) X-ray, (three) submillimeter, and (one) radio sources in the field. They were all in the primary sample.

With the color information from the optical and near-infrared identifications, we can divide 6.7 μm galaxies into three types. The GRASIL galaxy model predicts that red $B-I$ colors and blue $K-6.7$ μm colors can be used to isolate low-redshift early-type galaxies (type I). Red $B-K$ colors and red $I-6.7$ μm colors were used to select high-redshift early-type progenitors (type II), which can be regarded as ancestors of the type I galaxies. Blue $B-K$ colors and blue $I-6.7$ μm colors are an indicator of ongoing star formation (type III). The main contributors to the type III category would be late-type galaxies. The ratio of the three types was almost 1:1:1 in the 31 primary galaxies, while the supplementary galaxies have a higher fraction of type II galaxies.

In order to permit quantitative discussions, we estimated photometric redshifts for the 6.7 μm galaxies. Based on their good representations in the color-color plots, we used a limited set of SEDs in the GRASIL library for the fitting templates. A test of this photometric redshift estimation with a spectroscopic subsample suggested that they could be used as good redshift estimates. Although a few of them could be high-redshift outliers, the large errors in their photometric redshifts might be used as indicators.

Modulo the caveats on photometric redshifts, we found that deep 6.7 μm surveys were efficient in detecting high-redshift galaxies. The flux redshift relation of the primary 6.7 μm galaxies showed a high-redshift tail at fluxes below 30 μJy. A significant fraction of the photometric redshifts for the supplementary galaxies were $z > 1$, consistent with the dominance of type II galaxies among them. A $K < 20$ sample has low-redshift galaxies with $K > 18$ and $I-K < 2$, while our 6.7 μm sample does not include a population of such blue, low-mass galaxies.

Stellar masses were derived based on a tight correlation between rest-frame near-infrared luminosity and stellar mass. Stellar mass-to-light ratios were determined from fits to a limited set of template SEDs in the GRASIL library. With a hybrid conversion to stellar mass, using K luminosities at $z < 1$ and 6.7 μm luminosities at $z > 1$, we estimated stellar masses for the 6.7 μm galaxies. We found that some of the high-redshift 6.7 μm galaxies had stellar masses comparable to the typical stellar mass of local galaxies. However, the comoving space density of such massive galaxies is likely to be a decreasing function of redshift. The epoch-dependent stellar mass functions might suggest that more massive galaxies are rarer at higher redshifts. If our photometric redshifts are slight overestimates, this trend will be even stronger.

We derived the contributions of the 6.7 μm galaxies to the stellar mass density in the universe as a function of redshift. Given the narrow mass ranges, our estimates were obtained as simple summations of the detected sources. Our low-redshift value was almost consistent with the local value, suggesting that our sample includes major contributors to the low-redshift stellar mass density. At the same time, most of the mass assembly in galaxies should be finalized at this epoch ($z \sim 0.3$). The stellar mass density estimates become smaller at higher redshifts. This would be expected from the decrease in the high-redshift stellar mass functions; however, the density we compute for the highest redshift bin is almost comparable to the full mass range value for a rest-frame optical-selected sample. Note that our value includes contributions of dusty submillimeter galaxies. A full mass range sample of rest-frame near-infrared–selected galaxies will be necessary to estimate correct values of the stellar mass density taking into account any dusty population.

We are indebted to an anonymous referee for critical but kind and thorough comments. Y. S. would like to thank Toru Yamada, Joel Primack, Peter Eisenhardt, Mark Dickinson, and Alberto Franceschini for their encouragement at the ESO/Venice workshop on the mass of galaxies in 2001. He also acknowledges Masayuki Uemura and Nobuo Arimoto for their comments at the initial phases of this work. This research has been partly supported by JSPS Research Fellowships for Young Scientists. The analysis has been achieved with the IDL Astronomy Users Library maintained by Wayne Landsman. This research has made use of NASA's Astrophysics Data System Bibliographic Services.

APPENDIX

THE GRASIL SED LIBRARY

Granato and Silva introduced effects of graphite and silicate dust to an SED model of galaxies based on the stellar population synthesis method (Silva et al. 1998). Effects of dusty interstellar media are treated with a radiative transfer code. Thus, the GRASIL SEDs cannot be arbitrarily rescaled. The modeled SEDs include UIB emissions, which are believed to be caused by polycyclic aromatic hydrocarbon (PAH)

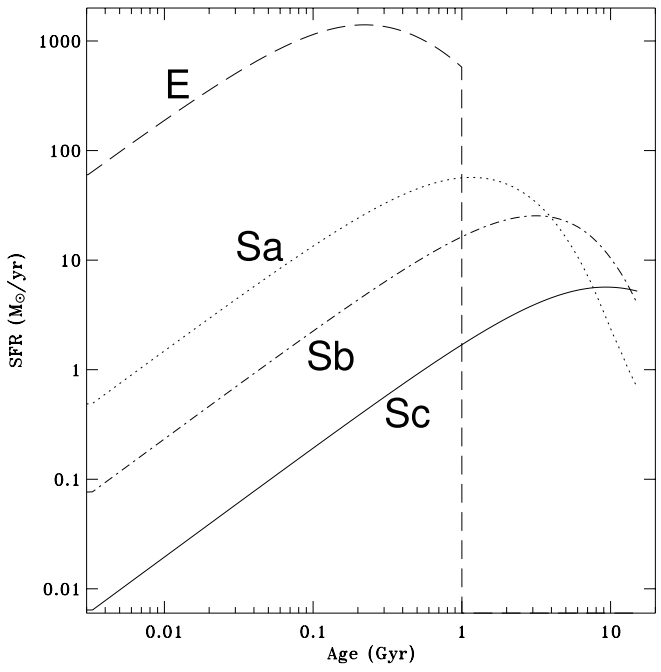

FIG. 14.—Star formation rates for the evolving E (*dashed lines*), Sa (*dotted lines*), Sb (*dot-dashed lines*), and Sc (*solid lines*) galaxies in the GRASIL library (Appendix) are shown as a function of age (*increasing from left to right*). After the age of 1 Gyr, the E galaxy was assumed to stop its star formation because of a galactic wind.

particles. A small suite of SEDs and executables to calculate SEDs are publicly available at the official GRASIL Web site.[10] The full details of the model can be traced at that site and the SED library itself is expanding. In order to avoid generating inadequate SEDs by using executables with excessive parameter sets, we have used just the author-proofed SED library in this paper. Here we describe the salient properties of two sets of SEDs in the library.

One is a set of evolving SEDs for four Hubble types in the local universe; E, Sa, Sb, and Sc. Elliptical galaxies are assumed to be formed in a monolithic collapse scenario. The classification of spiral galaxies is based on Solanes, Salvador-Solé, & Sanroma (1989). These SEDs span from UV to radio wavelengths. There are 12 ages for the E galaxy (0.1, 0.2, 0.4, 0.8, 1.5, 2, 3, 4, 5, 8, 11, and 13 Gyr) and 15 for the Sa, Sb, and Sc galaxies (1, 2, 3, 4, 5, 6, 7, 8, 9, 10, 11, 12, 13, 14, and 15 Gyr). Their star formation histories are assumed to be smooth, as shown in Figure 14. By setting a cosmology and a formation redshift, we can convert their age into redshift.

For stellar populations, Salpeter IMFs (Salpeter 1955) are assumed with mass limits of 0.15 and 120 $M_\odot$ for the E galaxy and 0.10 and 100 $M_\odot$ for the Sa, Sb, and Sc galaxies, respectively. Using a K-band luminosity function for local galaxies, Cole et al. (2001) have provided a stellar mass function for a Salpeter IMF with mass limits of 0.1 and 125 $M_\odot$. The characteristic stellar mass for this stellar mass function becomes $M^*_{\rm star} = 1.7 \times 10^{11}\ M_\odot$ for our adopted cosmology. With this unit, the GRASIL E, Sa, Sb, and Sc galaxies with a formation redshift of $z_f = 2$ have stellar masses of $\sim$3, $\sim$0.8, $\sim$0.7, and $\sim$0.2 $M^*_{\rm star}$, respectively, at $z = 0$. All the stellar mass estimates with the GRASIL SEDs in this paper were normalized to a Salpeter IMF with mass limits of 0.1 and 125 $M_\odot$.

The other set of SEDs contains fitted templates of nearby galaxies, which are detailed in Silva et al. (1998). The model parameters were chosen to represent SEDs for starburst galaxies (M82, NGC6090, and Arp220), normal galaxies (M51, M100, and NGC6946), and a giant elliptical galaxy. The wavelength range is shorter than the evolving SEDs above, from UV to submillimeter.

We used all the SEDs above to derive photometric redshifts. To obtain stellar masses, we only utilized the evolving SEDs, since some of the fitted templates lack stellar mass information. Model predictions based on the evolving SEDs are shown in some plots, though the Sb SED was omitted to avoid overcrowding.

[10] See http://web.pd.astro.it/granato/grasil/grasil.html.

REFERENCES

Altieri, B., et al. 1999, A&A, 343, L65
Aussel, H., Cesarsky, C. J., Elbaz, D., & Starck, J. L. 1999, A&A, 342, 313
Avni, Y. 1976, ApJ, 210, 642
Barger, A. J., Cowie, L. L., Mushotzky, R. F., & Richards, E. A. 2001, AJ, 121, 662
Barger, A. J., Cowie, L. L., & Sanders, D. B. 1999, ApJ, 518, L5
Barger, A. J., Cowie, L. L., Sanders, D. B., Fulton, E., Taniguchi, Y., Sato, Y., Kawara, K., & Okuda, H. 1998, Nature, 394, 248
Bolzonella, M., Miralles, J.-M., & Pelló, R. 2000, A&A, 363, 476
Brinchmann, J., & Ellis, R. S. 2000, ApJ, 536, L77
Carilli, C. L., & Yun, M. S. 2000, ApJ, 530, 618
Carroll, S. M., Press, W. H., & Turner, E. L. 1992, ARA&A, 30, 499
Cesarsky, C. J., et al. 1996, A&A, 315, L32
Cohen, J. G. 2002, ApJ, 567, 672
Cole, S., et al. 2001, MNRAS, 326, 255
Condon, J. J., Cotton, W. D., Greisen, E. W., Yin, Q. F., Perley, R. A., Taylor, G. B., & Broderick, J. J. 1998, AJ, 115, 1693
Cowie, L. L., Gardner, J. P, Hu, E. M., Songaila, A., Hodapp, K.-W., & Wainscoat, R. J. 1994, ApJ, 434, 114
Cowie, L. L., Hu, E. M., & Songaila, A. 1995, AJ, 110, 1576
Cowie, L. L., Songaila, A., Hu, E. M., & Cohen, J. G. 1996, AJ, 112, 839
Dickinson, M., Papovich, C., Ferguson, H. C., & Budavári, T. 2003, ApJ, 587, 25
Drory, N., Bender, R., Snigula, J., Feulner, G., Hopp, U., Maraston, C., Hill, G. J., & de Oliveira, C. M. 2001, ApJ, 562, L111
Elbaz, D., et al. 1999, A&A, 351, L37
Flores, H., et al. 1999a, A&A, 343, 389
———. 1999b, ApJ, 517, 148
Fontana, A. J., et al. 2003, ApJ, 594, L9
Franceschini, A., Aussel, H., Cesarsky, C. J., Elbaz, D., & Fadda, D. 2001, A&A, 378, 1
Franceschini, A., et al. 2003, A&A, 403, 501
Genzel, R., & Cesarsky, C. J. 2000, ARA&A, 38, 761
Giallongo, E., D'Odorico, S., Fontana, A., Cristiani, S., Egami, E., Hu, E., & McMahon, R. G. 1998, AJ, 115, 2169
Hasinger, G. 2000, *ISO* Survey of a Dusty Universe, ed. D. Lemke, M. Stickel, & K. Wilke (Berlin: Springer), 423
Hogg, D. W. 1999, preprint (astro-ph/9905116)
Hogg, D. W., et al. 1998, AJ, 115, 1418
Hughes, D. H., et al. 1998, Nature, 394, 241
Iwasawa, K. 1999, MNRAS, 302, 96
Kessler, M. F., et al. 1996, A&A, 315, L27
Maihara, T., et al. 2001, PASJ, 53, 25
Mann, R. G., et al. 1997, MNRAS, 289, 482
Metcalfe, L., et al. 2003, A&A, 407, 791
Metcalfe, N., Shanks, T., Campos, A., McCracken, H. J., & Fong, R. 2001, MNRAS, 323, 795
Mushotzky, R. F., Cowie, L. L., Barger, A. J., & Arnaud, K. A. 2000, Nature, 404, 459
Oliver, S., et al. 2002, MNRAS, 332, 536
Salpeter, E. E. 1955, ApJ, 121, 161
Salucci, P., & Persic, M. 1999, MNRAS, 309, 923
Sato, Y., Cowie, L. L., Kawara, K., Taniguchi, Y., Sofue, Y., Matsuhara, H., & Okuda, H. 2002, ApJ, 578, L23
Sato, Y., et al. 2003, A&A, 405, 833
Sawicki, M. 2002, AJ, 124, 3050
Serjeant, S. B. G., et al. 1997, MNRAS, 289, 457
Silva, L., Granato, G. L., Bressan, A., & Danese, L. 1998, ApJ, 509, 103
Solanes, J. M., Salvador-Solé, E., & Sanroma, M. 1989, AJ, 98, 798
Songaila, A., Cowie, L. L., Hu, E. M., & Gardner, J. P. 1994, ApJS, 94, 461
Steidel, C. C., Adelberger, K. L., Giavalisco, M., Dickinson, M., & Pettini, M. 1999, ApJ, 519, 1
Takeuchi, T. T., Yoshikawa, K., & Ishii, T. T. 2000, ApJS, 129, 1
Taniguchi, Y., et al. 1997, A&A, 328, L9
White, R. L., Becker, R. H., Helfand, D. J., & Gregg, M. D. 1997, ApJ, 475, 479